



### Available online at www.sciencedirect.com

# **ScienceDirect**

Geochimica et Cosmochimica Acta 195 (2016) 29-67

# Geochimica et Cosmochimica Acta

www.elsevier.com/locate/gca

# Quantifying chemical weathering rates along a precipitation gradient on Basse-Terre Island, French Guadeloupe: New insight from U-series isotopes in weathering rinds

Jacqueline M. Engel<sup>a</sup>, Lin Ma<sup>a,\*</sup>, Peter B. Sak<sup>b</sup>, Jerome Gaillardet<sup>c</sup>, Minghua Ren<sup>d</sup>, Mark A. Engle<sup>e</sup>, Susan L. Brantley<sup>f</sup>

<sup>a</sup> Department of Geological Sciences, University of Texas at El Paso, El Paso, TX, USA <sup>b</sup> Department of Earth Sciences, Dickinson College, Carlisle, PA, USA <sup>c</sup> Institut de Physique du Globe de Paris, Paris, France <sup>d</sup> Department of Geoscience, University of Nevada at Las Vegas, Las Vegas, NV, USA <sup>e</sup> United States Geological Survey, Reston, VA, USA f Earth and Environmental Systems Institute and Department of Geosciences, Pennsylvania State University, University Park, PA, USA

Received 13 August 2015; accepted in revised form 27 August 2016; Available online 13 September 2016

### Abstract

Inside soil and saprolite, rock fragments can form weathering clasts (alteration rinds surrounding an unweathered core) and these weathering rinds provide an excellent field system for investigating the initiation of weathering and long term weathering rates. Recently, uranium-series (U-series) disequilibria have shown great potential for determining rind formation rates and quantifying factors controlling weathering advance rates in weathering rinds. To further investigate whether the U-series isotope technique can document differences in long term weathering rates as a function of precipitation, we conducted a new weathering rind study on tropical volcanic Basse-Terre Island in the Lesser Antilles Archipelago. In this study, for the first time we characterized weathering reactions and quantified weathering advance rates in multiple weathering rinds across a steep precipitation gradient. Electron microprobe (EMP) point measurements, bulk major element contents, and U-series isotope compositions were determined in two weathering clasts from the Deshaies watershed with mean annual precipitation (MAP) = 1800 mm and temperature (MAT) = 23 °C. On these clasts, five corerind transects were measured for locations with different curvature (high, medium, and low) of the rind-core boundary. Results reveal that during rind formation the fraction of elemental loss decreases in the order:  $Ca \approx Na > K \approx Mg > Si \approx Al > Zr \approx Ti \approx Fe$ . Such observations are consistent with the sequence of reactions after the initiation of weathering: specifically, glass matrix and primary minerals (plagioclase, pyroxene) weather to produce Fe oxyhydroxides, gibbsite and minor kaolinite.

Uranium shows addition profiles in the rind due to the infiltration of U-containing soil pore water into the rind as dissolved U phases. U is then incorporated into the rind as Fe-Al oxides precipitate. Such processes lead to significant U-series isotope disequilibria in the rinds. This is the first time that multiple weathering clasts from the same watershed were analyzed for U-series isotope disequilibrian and show consistent results. The U-series disequilibria allowed for the determination of rind formation ages and weathering advance rates with a U-series mass balance model. The weathering advance rates generally decreased with decreasing curvature:  $\sim$ 0.17  $\pm$  0.10 mm/kyr for high curvature,  $\sim$ 0.12  $\pm$  0.05 mm/kyr for medium curvature, and  $\sim 0.11 \pm 0.04$ ,  $0.08 \pm 0.03$ ,  $0.06 \pm 0.03$  mm/kyr for low curvature locations. The observed positive correlation

<sup>\*</sup> Corresponding author. E-mail address: lma@utep.edu (L. Ma).

between the curvature and the weathering rates is well supported by predictions of weathering models, i.e., that the curvature of the rind-core boundary controls the porosity creation and weathering advance rates at the clast scale.

At the watershed scale, the new weathering advance rates derived on the low curvature transects for the relatively dry Deshaies watershed (average rate of 0.08 mm/kyr; MAP = 1800 mm and MAT = 23 °C) are  $\sim$ 60% slower than the rind formation rates previously determined in the much wetter Bras David watershed ( $\sim$ 0.18 mm/kyr, low curvature transect; MAP = 3400 mm and MAT = 23 °C) also on Basse-Terre Island. Thus, a doubling of MAP roughly correlates with a doubling of weathering advance rate. The new rind study highlights the effect of precipitation on weathering rates over a time scale of  $\sim$ 100 kyr. Weathering rinds are thus a suitable system for investigating long-term chemical weathering across environmental gradients, complementing short-term riverine solute fluxes.

Keywords: U-series isotopes; Weathering rinds; Weathering rates; Precipitation; French Guadeloupe

#### 1. INTRODUCTION

Quantifying weathering rates for small tropical volcanic islands is of particular interest in understanding weathering processes at global scales. For example, tropical volcanic islands weather at rapid rates due to the reactive nature of the volcanic rocks and hot and humid climate (Louvat and Allègre, 1997; Gaillardet et al., 1999, 2011; Chadwick et al., 1999; Dessert et al., 2003; Derry et al., 2005; Goldsmith et al., 2010; Lloret et al. 2011). Weathering on small volcanic islands, despite covering only a small portion of Earth's surface, accounts for up to ~25% of CO2 consumed by global silicate weathering (Dessert et al., 2003). The rapid removal of weathering products by rivers generates extremely high chemical denudation fluxes (Goldsmith et al., 2010; Gaillardet et al., 2011) and high sediment yields (Carpentier et al., 2008) on small volcanic islands. Many researchers have investigated how chemical weathering rates respond to changes in climate, landscape and tectonic regimes by measuring riverine solute fluxes. For example, previous studies have documented a strong positive correlation between riverine solute fluxes and river runoff or mean annual precipitation (MAP) on volcanic islands, highlighting particularly the important control of water cycle and hydrology on chemical weathering and CO<sub>2</sub> consumption (e.g., Goldsmith et al., 2010; Gaillardet et al., 2011; Eiriksdottir et al., 2013).

However, the use of riverine solute fluxes to infer weathering rates has several limitations. First, the measured solute fluxes correspond to weathering rates in catchments if the residence time of water in catchment systems is known. These rates are snapshots in time that may only document the current climate. Their potential use to investigate the influence of climate patterns over long timescales is limited. Second, the calculation of riverine solute fluxes involves the use of river runoff values. Specifically, the riverine solute fluxes are solute concentrations multiplied by river runoff values, and the fact that solute concentrations can be chemostatic and vary much less than runoff values (Gaillardet et al., 2011) may introduce an autocorrelation between solute fluxes and runoff. Therefore the actual relationship between weathering fluxes and river runoff (or MAP) may be complicated. Third, the measured river chemical fluxes are generally normalized to the geographic area of watersheds, not the actual reactive mineral surface area where chemical

reactions occur. Hence, a comparison of weathering rates measured at different watersheds should be reconciled by approaches such as introducing the surface roughness or flow path factors (e.g. Navarre-Sitchler and Brantley, 2007; Maher, 2010). One way to circumvent some of these complications is to measure directly long-term chemical weathering rates in solid-state weathering products.

Critical Zone processes such as chemical weathering and physical disaggregation transform bedrock into saprolite and soil. During the transformation, some rock fragments within regolith may alter and form porous alteration rinds surrounding unweathered core materials (collectively known as a weathering clast). Rind formation initiates at the core-rind boundary as unweathered material is exposed to infiltrating pore water. The water carries weathering reagents such as H<sup>+</sup> and dissolved O<sub>2</sub> that initiate release of soluble elements (e.g., Mg, Ca, Na, and K). The resulting rind is generally composed of oxides and secondary minerals enriched in immobile elements (e.g. Ti, Fe, Th, and Al). Overtime, the rind thickness increases as the core-rind boundary advances into the core. In some instances, the outermost layer of rind may disintegrate into surrounding soil. Weathering rinds provide a unique and excellent small-scale system for investigating the initiation of weathering reactions, because most large-scale field systems such as soil profiles or watersheds may be impacted by additional processes such as physical erosion, mixing, variations in fracture density, parent material compositional heterogeneity, and dust inputs.

Previous alteration rind research efforts have focused on using geometry and thickness of weathering rinds as a relative age indicator of terraces (e.g., Cernohouz and Solc, 1966; Porter, 1975; Colman and Pierce, 1981; Kirkbride and Bell, 2010), and have studied changes in the chemistry and mineralogy across the core-rind boundary to characterize chemical reactions, porosity development, and environmental conditions (Colman, 1982a,b; Sak et al., 2004; Graham et al., 2010; Yoshida et al., 2011). Some researchers have developed mathematical models to simulate porosity development, phase transformation, and advance rates of core-rind boundary during rind formation (Oguchi and Matsukura, 2000; Gordon and Dorn, 2005; Hausrath et al., 2008; Navarre-Sitchler et al., 2009, 2011; Lebedeva et al., 2010, 2015; Rossi and Graham, 2010; Sak et al., 2010; Reeves and Rothman, 2014).

Recently, a uranium-series (U-series) chronometer in weathering rinds has been successfully applied to determine rates of weathering rind formation and to quantitatively understand factors controlling weathering advance rates at the clast scale (Pelt et al., 2008; Ma et al., 2012). The radioactive U-series isotopes (e.g., <sup>238</sup>U, <sup>234</sup>U, and <sup>230</sup>Th) are characterized by various half-lives and distinct geochemical properties in geological environments (e.g., Ivanovich and Harmon, 1992; Bourdon et al., 2003). Understanding the mobility of U-series isotopes at Earth's surface has led to recent advancements in U-series as a chronometer to constrain the rates and duration of chemical weathering in soils, rinds, and riverine sediments with time scales ranging from several kyr to 1 Myr (Sarin et al., 1990; Chabaux et al., 2003a, 2008 and references therein; Dosseto et al., 2006, 2008a,b, 2014; Granet et al., 2007, 2010; Pelt et al., 2008; Ma et al., 2010, 2012). The two recent weathering rind studies (Pelt et al., 2008; Ma et al., 2012) documented that during the formation of basaltic/andesitic weathering rinds in Costa Rica and Guadeloupe, soil pore waters transported dissolved U (238U and <sup>234</sup>U) into the rind, in addition to leaching U from the rind as previously expected. The mechanism of U deposition in rinds is likely related to sorption along with the formation of secondary minerals such as Fe-oxides after creation of porosity in these low porosity rocks. The accumulation of U and its subsequent modification of U-series decay chain with time has provided a tool to determine radiometric rind

formation ages and weathering rates, highlighting the use of U-series isotopes as a highly desired geochronometer for chemical weathering studies, especially for tropical volcanic regions (Pelt et al., 2008; Ma et al., 2012).

To investigate whether the U-series isotope technique can further document differences in rind formation rates as a function of precipitation over long time scales, we have conducted a new rind study on Basse-Terre Island in the Guadeloupe Archipelago (Fig. 1). Basse-Terre is a tropical volcanic island characterized by a steep precipitation gradient. In this study we focus on multiple weathering rinds collected from the northern relatively dry part of the island (Deshaies watershed: MAP = 1800 mm; mean annual temperature, or MAT = 23 °C), an ideal site to compare to the previously studied site in the wet central island (Bras David watershed: MAP = 3400 mm;  $MAT = 23 \,^{\circ}\text{C}$ ) (Sak et al., 2010; Ma et al., 2012). Weathering clasts and bedrock were systematically characterized by petrographic, bulk chemical, electron microprobe (EMP), and U-series isotope analyses. This study provides new direct evidence that Useries isotopic systematics in weathering rinds chosen along a gradient in MAP elucidate the control of precipitation on long term weathering rates. Results from this study also reveal new details about how U was immobilized during rind formation as well as important controlling factors on rind formation rates at the clast scale, i.e. curvature of rind-core boundary, reactive phases, and porosity development. Weathering advance rates determined at the clast

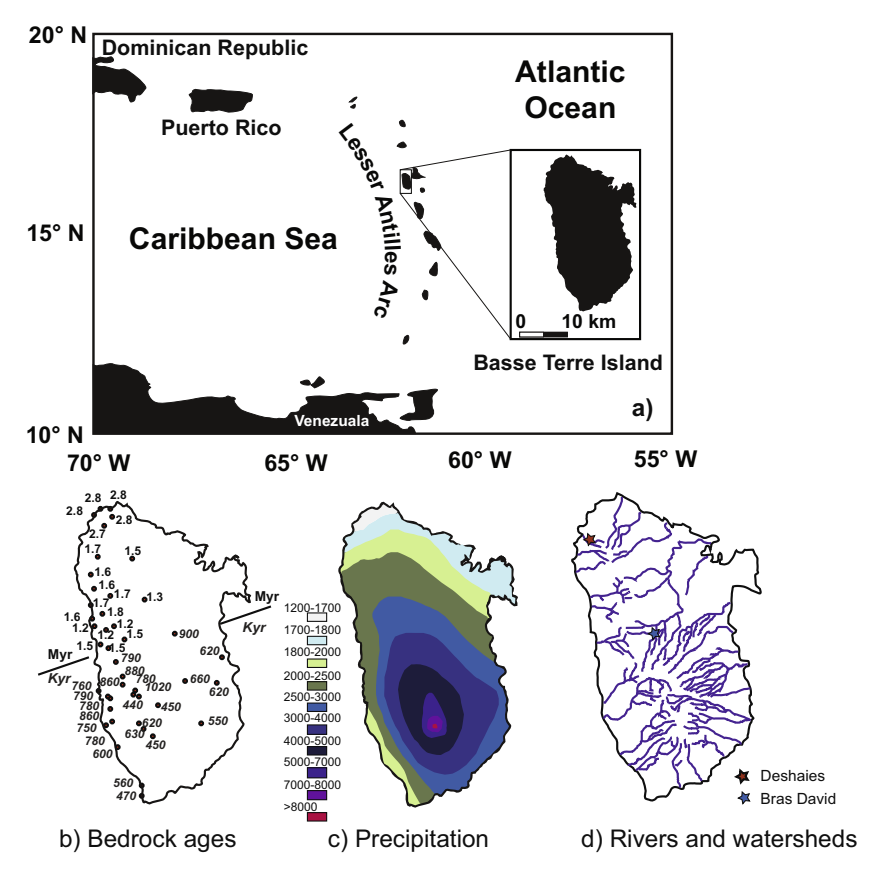


Fig. 1. (a) Location map of Basse-Terre Island in French Guadeloupe; (b) Bedrock ages (Samper et al., 2007); (c) annual precipitation (mm yr<sup>-1</sup>; data from Metro France); (d) Rivers and watersheds: locations of Deshaies and Bras David are indicated.

scale also reveal important information to assess the role of surface roughness and flow path factors when compared to weathering rates determined at watershed scales.

### 2. BACKGROUND OF BASSE-TERRE ISLAND

# 2.1. Geological setting and climate

Basse-Terre Island is a part of the French Guadeloupe archipelago in the Lesser Antilles arc (Fig. 1a), which was generated during subduction of the South American plate beneath the Caribbean plate (e.g. Jordan, 1975; Hawkesworth and Powell, 1980). Despite its small exposed surface (850 km²), Basse-Terre is a suitable location for exploring the effect of precipitation on rates of chemical weathering and denudation because of the steep gradients in the bedrock ages, relief, and precipitation (Fig 1b, c, d; https://morpho.ipgp.fr/Obsera).

Basse-Terre Island is comprised of relatively homogenous andesitic to basaltic-andesitic volcanic materials that form lava flows, lava domes, pyroclastic deposits, and volcanic-clastic debris flows (Samper et al., 2007). The island can be divided into four main structural zones corresponding to volcanic massifs of younger age southward (Fig. 1b). The Basal Complex occupies the extreme northern part of the island and is characterized by Pliocene volcanism (2.8–2.6 Ma). The Septentrional Chain occupies most of the northern part of Basse-Terre characterized by ages from 1.8 to 1.15 Ma. The central part of the island is composed of the Axial Chain with volcanic material dated from 1 to 0.4 Ma. The southernmost part is the Grande Decouverte Volcanic Complex characterized by <0.2 Ma volcanism with the most recent activity at La Soufriere volcano (8.5 ka to present) (Samper et al., 2007; Lahitte et al., 2012; Ricci et al., 2015).

Topographic variability on the island closely mimics the bedrock age, with high relief and steep slopes in the young and active southern areas and lower relief and gentler slopes in the much older and more stable northern part. Because of the north–south trending topographic divide and the prevailing winds from the east, the average annual precipitation (MAP) on Basse-Terre Island, ranging from 1200 to >8000 mm, is largely controlled by an orographic effect (Fig. 1c). Notably, the east and south coasts receive high MAP (>4000 mm), with the highest values at the summit of La Soufrière massif, and the leeward west and north coasts generally receive MAP < 2000 mm. Basse-Terre Island is thus characterized by a steep gradient in precipitation. At the same time, the island experiences a near constant mean annual temperature of 23 °C at sea level.

# 2.2. Chemical weathering fluxes across precipitation gradient

The abundant precipitation creates a dense network of rivers flowing over the volcanic materials and draining to the Atlantic Ocean and the Caribbean Sea (Fig. 1d). These rivers transport a substantial solute load: catchment-wide chemical weathering fluxes have been calculated in 28 major rivers on the island and range from 39 to 427 t/km<sup>2</sup>/yr, among the highest fluxes calculated on Earth

(Gaillardet et al., 2011; Lloret et al., 2013; Dessert et al., 2015). These studies have also documented a strong positive correlation between riverine solute fluxes and MAP (or runoff), or more precisely two correlations: one for rivers impacted by hydrothermal activity and one for rivers non impacted by hydrothermal inputs and having (at a given runoff) lower solute fluxes. Gaillardet et al. (2011) proposed that these correlations (particularly for the nonhydrothermally impacted rivers) essentially reflect the fact that the solute concentration range over the N-S gradient is much less important than the range of runoff changes (a regional chemostatic behavior). These authors associated the runoff-solute fluxes correlation with a CO<sub>2</sub> regulating mechanism, i.e., that volcanic activity generates relief that promotes high orographic precipitation and relatively permeable infiltration regimes, which in turn result in elevated chemical denudation rates and high rates of atmospheric CO<sub>2</sub> consumption. Many researchers have promoted the notion that tectonic uplift accelerates chemical weathering by increasing physical erosion rates (e.g., Chamberlin, 1898; Raymo and Ruddiman, 1992; Jacobson et al., 2003; Hren et al., 2007; Hilley and Porder, 2008; Hilley et al., 2010), providing an important mechanism to regulate atmospheric CO<sub>2</sub> contents in addition to the well-known temperature-related feedback mechanism (e.g., Walker et al., 1981; Berner et al., 1983). This new mechanism proposed by Gaillardet et al. (2011) focuses on the importance of the water cycle and hydrology in controlling chemical weathering and CO<sub>2</sub> consumption (e.g., Godsey et al., 2009; Eiriksdottir et al., 2013). The strong positive correlation between riverine solute fluxes and MAP makes Basse-Terre an ideal study site to further investigate whether U-series disequilibria in weathering rinds can document changes of long term weathering rates as a function of MAP.

### 3. METHODS

### 3.1. Site description and sample collection

The study site is located in a quarry operated by Societe Antillaise de Granulats (SADG) within the Deshaies watershed in the northwestern portions of Basse-Terre (N 16° 18.635' W 61°46.601', Elevation 248 m; Fig. 2a). The andesitic bedrock at this site formed ~1.6 Ma (Samper et al., 2007). The climate within the watershed is tropical and humid (MAP = 1800 mm and MAT = 23 °C). Vegetation cover in this area is classified as a semi-deciduous and seasonal evergreen forest (Rousteau, 1996). Thick soil and saprolite zones have developed on the andesitic bedrock (Fig. 2b), with predominant soil orders as oxisols with high montmorillonite and kaolinite content (Ndaviragije and Delvaux, 2004). The Deshaies watershed provides a relatively "dry" study site, compared to the previously studied wetter Bras David watershed in the central island (MAP ~3400 mm; MAT: 23 °C; Sak et al., 2010; Ma et al., 2012). The vegetation of the Bras David watershed is characterized as a mountain rain forest and soils are thick oxisols with halloysites and iron oxides (Buss et al., 2010; Lloret et al., 2011).

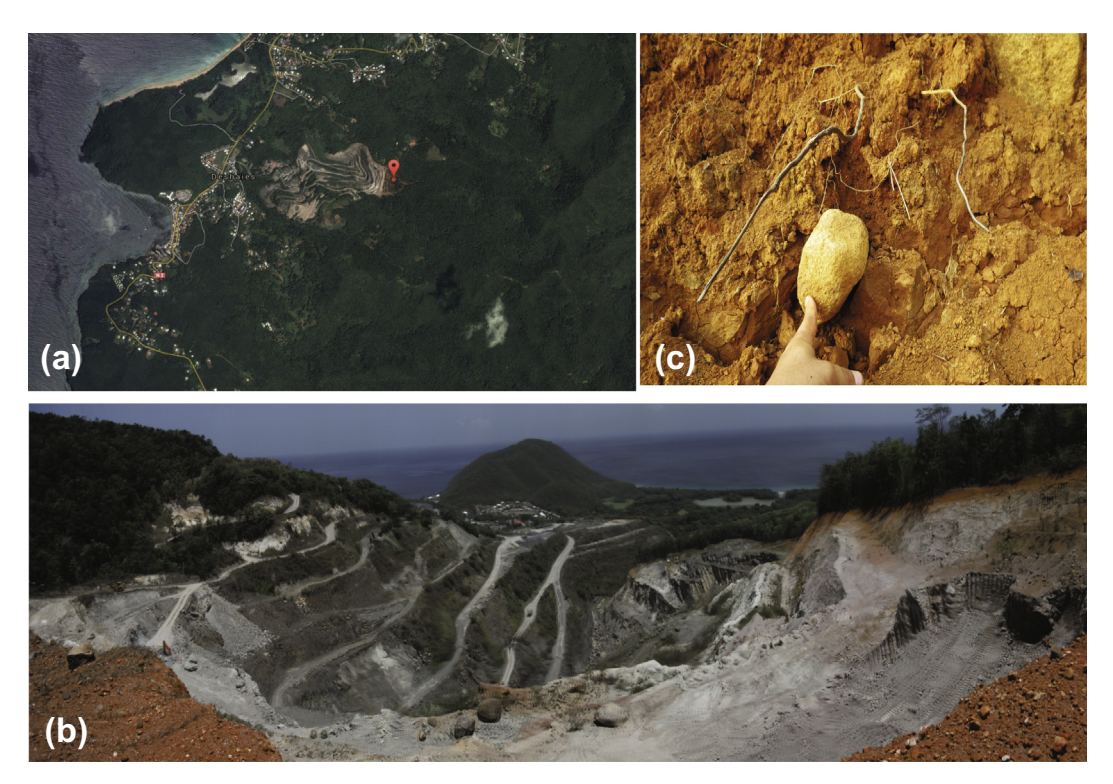


Fig. 2. (a) Satellite image of study area in Deshaies, Basse-Terre Island (Image from Google Earth); (b) View of the quarry site operated by Societe Antillaise de Granulats (SADG), near Deshaies; (c) Photo of the soil profile in the field from which clast samples were collected.

Quarrying activities have exposed a thick weathering profile (Fig. 2b). The profile sequence starts from the bottom as fresh dark grey andesite, exposed at the base of the quarry, to a ~40 m thick layer of light grey weathered andesite. The weathered bedrock grades upward into  $\sim$ 10–20 m thick white to brown highly weathered saprolite. The saprolite is capped by  $\sim 1-5$  m thick red brown soil. At the sampling location near the top of the quarry, multiple weathering clasts were collected from a soil profile near a road cut (Fig. 2c). Because the topsoil profile has been disturbed by the road construction, the exact soil depth of the clasts was not available. Depth was therefore estimated to be  $\sim 1$  m based on comparison of soil matrix color with a nearby undisturbed soil profile. In the field, the weathering clasts were distinguished from the surrounding soil by color: the clast is brownish yellow (Munsell Color Notation 10YR 7/6) in contrast to the yellowish red (Munsell Color Notation 5YR 4/4) soil matrix (Fig. 2c). After sample collection, the clasts were wrapped in aluminum foil and masking tape at the field site to prevent loss of the friable rind material during transportation. In the laboratory, the clasts were immersed in molten wax before complete unwrapping to preserve rind structure. The clasts were removed from the wax bath and allowed to cool for 24 h, before the excess wax on the exterior was removed by heating to 55 °C for 8 h in a laboratory oven. The wax-impregnated clasts were separated into two sections by cutting a vertical section along the major axis (Fig. 3). Thin section billets were cut from one half of the clasts and samples for chemical and isotopic analyses were collected from the other half.

The curvature of the core-rind boundary on clast AN-14-7.6 (Fig. 3) was described according to procedures in Sak

et al. (2010). Briefly, the clast was cut into two sections vertically along the major axis. The cut section was imaged using a high-resolution scanner. The core–rind boundary was defined with a Matlab script as a series of (x, y) points on the scanned image where the color-change gradient between the core and rind material was highest (Fig. 3). The curvature  $(\kappa)$  of this boundary y(x) was calculated using the following definition:  $\kappa = y''/(1+(y')^2)^{3/2}$ , where primes denote derivatives with respect to x. With this standard definition of curvature in two dimensions, only straight lines and circles have constant curvature. Note that we have defined the curvature as the curvature of the interface imaged in the plane of the clast slice (e.g., in two dimensions), and not the Laplacian of the core-rind interface in three-dimension (e.g. Lebedeva et al., 2015).

Rind and core samples for chemical and isotopic analyses were obtained by drilling powder material using a 3.175 mm diameter carbide-tipped bit. Clast sample AN-14-7.6 was drilled along three transects perpendicular to the core-rind boundary that are characterized by high, medium and low curvature, due to the oblate geometry (Fig. 3): two samples were collected from the core, five across the rind along a low curvature segment (7.6 L), four across the rind along a medium curvature segment (7.6 M), and three across the rind along a high curvature segment (7.6 H) of the core-rind boundary. Clast sample AN-14-7.5 was drilled along two transects perpendicular to the low curvature core-rind boundary (Fig. 3): one sample was collected from the core, five across the rind along a low curvature segment (7.5 L1), four across the rind along another low curvature segment (7.5 L2). At each drilling location, two small cylinders were cored: one for major

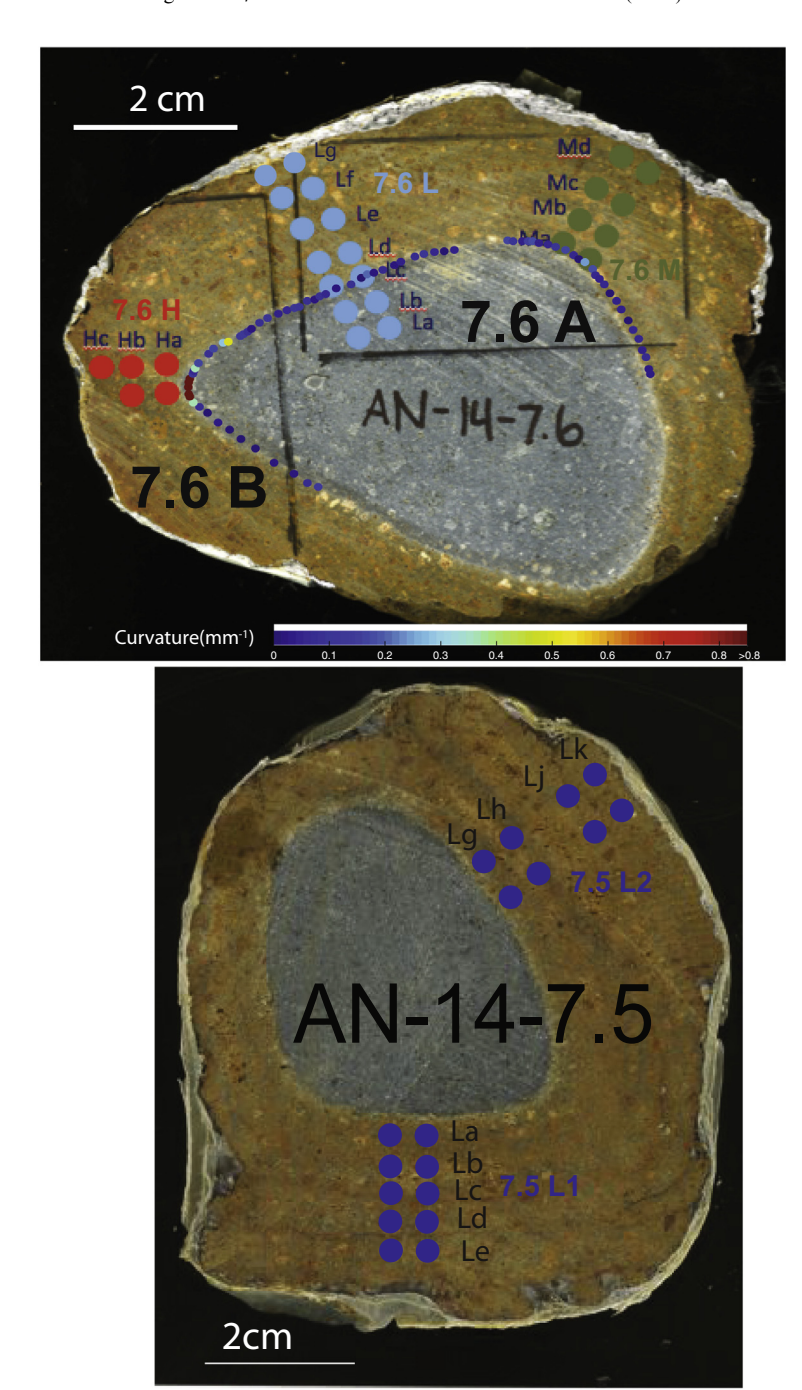


Fig. 3. Photographs of cut sections of the weathering clasts (AN-14-7.6 and AN-14-7.5). The visually defined core-rind boundary is color-coded for curvature (mm<sup>-1</sup>) for AN-14-7.6. Note that during removal of the clasts from the soil matrix, small portions of the outer rind corners disaggregated from both clasts. Two black boxes (7.6A and 7.6B) indicate the locations where detailed images and chemical compositions are scanned with EMP for clast AN-14-7.6. Drilled sample locations for the core and the rind transects on clast AN-14-7.6 (low, medium, and high curvature sites, labeled as 7.6 L, 7.6 M, and 7.6 H) and on clast AN-14-7.5 (two low curvature sites, labeled as 7.5 L1 and 7.5 L2) are indicated. For each sample location, two pits were drilled: one for major element analysis and one for U-series isotope analysis. (For interpretation of the references to colour in this figure legend, the reader is referred to the web version of this article.)

element concentration analysis and one for U-series isotope analysis. Additional parent material was sampled and prepared for major element and mineralogy analysis by grinding several fresh andesite samples obtained from the deepest level of the quarry, approximately 100 m below the clast sample site.

# 3.2. Electron Microprobe analysis

Spatial changes in the bulk major element contents across the core-rind boundary of clast AN-14-7.6 was constrained using a JEOL electron microprobe (EMP) model JXA-8900 at the University of Nevada Las Vegas (UNLV)

with a  $\sim$ 40–60 µm spatial resolution. The EMP spot size is  $\sim$ 20 µm, larger than the crystal sizes in the groundmass but smaller than most phenocrysts in the clast. The analyses were conducted along three ~15 to 25 mm-long EMP profiles, oriented at a high angle to the visually-defined corerind boundary on clast AN-14-7.6. The three segments of the core-rind boundary were characterized by low, medium and high curvature, respectively. The EMP profiles were close to the drilled rind transects (Fig. 3). The EMP analysis was standardized with mineral and glass standards from the UNLV collection. Instrumental parameters were identical in calibration and measurement of unknowns: 15 kV accelerating voltage, 10 nA beam current, 20 µm beam size, and 30 s peak counting times. The analytical precision was estimated to be 1% for the EMP analyses including Ti. Si. Al. Ca, Mg, Na, K, Fe, Mn, and P. Backscattered electron (BSE) images and X-ray element maps (such as Ca, Mg, Na, K, Fe, Al, and Si) were also produced on both thin sections. X-ray element maps were completed using the following beam conditions: 15 kV, 50 nA, focused beam and stage mode for whole thin section maps.

# 3.3. Major element chemical analysis

Bulk elemental contents (Al, Ca, Mg, Na, K, Fe, Ti, Si, Mn, and P) in drilled samples for clast AN-14-7.6 and AN-14-7.5 were determined through chemical analysis. These samples were digested by Li metaborate fusion and analyzed on a Perkin–Elmer 5300DV inductively coupled plasma-atomic emission spectrometer (ICP-AES) in the Pennsylvania State University Laboratory for Isotopes and Metals in the Environment. The samples were analyzed along with USGS standards including Columbia River (BCR-1) and Hawaiian Volcano Observatory (BHVO-1) basalts for quality assessment. Based on the results of these USGS standards, the analytical precision was estimated to equal 2–5% for the ICP-AES analyses, except for P where analytical reproducibility is generally lower because it is typically present in very low concentrations.

### 3.4. U-series isotope analysis

U and Th concentrations and isotopic ratios in drilled samples for clast AN-14-7.6 and AN-14-7.5 were determined at the University of Texas at El Paso. About 20–100 mg of sample powder were weighed out and spiked with a mixed artificial <sup>233</sup>U–<sup>229</sup>Th tracer (<sup>233</sup>U was acquired from the New Brunswick Laboratory and <sup>229</sup>Th was from the National Institute of Standards and Technology). Samples were then fully dissolved using a two-step procedure using HNO<sub>3</sub>-HF and HCl-H<sub>3</sub>BO<sub>3</sub> acids. U and Th were separated from solution and purified using conventional cation exchange chromatography in a class-100 clean room following Pelt et al. (2008) and Ma et al. (2012). U concentrations and isotopic ratios (<sup>234</sup>U/<sup>238</sup>U and <sup>233</sup>U/<sup>238</sup>U) were measured on a Nu Plasma MC-ICP-MS using ~50 ng of U per sample. The standard-sample bracketing technique (with NBL 145B as the U bracketing solution) was used to correct for mass discrimination and drifting of ion counter/Faraday cup gains during measurements (e.g., Sims

et al., 2010). Relative internal uncertainties on U isotope ratios and U concentrations were ~0.5%. USGS rock reference standard BCR-2 was analyzed multiple times along with samples for data quality assurance. Measured values for BCR-2 were:  $(^{234}\text{U}/^{238}\text{U}) = 1.003 \pm 0.003$  and U concentration =  $1.700 \pm 0.025$  ppm (n = 3); both are consistent with reference values: BCR-2 ( $^{234}\text{U}/^{238}\text{U}$ ) = 1.000 ± 0.005 and U concentration =  $1.69 \pm 0.02$  ppm (Sims et al., 2010). U procedural blanks were  $\sim$ 20 pg. Th concentrations and isotope ratios (<sup>229</sup>Th/<sup>232</sup>Th and <sup>230</sup>Th/<sup>232</sup>Th) were measured on the same instrument using  $\sim$ 60 ng of Th per sample, with an in-house  $^{229-230-232}$ Th solution as the bracketing standard. The in-house Th solution was calibrated with IRMM 035 and IRMM 036 Th standards. During the inhouse Th solution calibration, <sup>229</sup>Th/<sup>232</sup>Th ratios were measured by individually determining ion counter/Faraday cup gains with a diluted <sup>232</sup>Th solution. To account for the tailing effect of <sup>232</sup>Th on <sup>230</sup>Th, ion counts were measured at mass 229.5 and mass 230.5 and corrected from the ion counts at mass 230 during both standard and sample analysis. Relative internal uncertainties on Th isotope ratios and Th concentration were  $\sim$ 1%. Measured values for BCR-2 were:  $(^{230}\text{Th}/^{232}\text{Th}) = 0.881 \pm 0.002$  and Th concentration =  $5.88 \pm 0.05$  ppm (n = 3); both agree with reference values: BCR-2 ( $^{230}$ Th/ $^{232}$ Th) =  $0.877 \pm 0.003$  and Th concentration =  $5.88 \pm 0.03$  ppm (Sims et al., 2010). Th procedural blanks were  $\sim$ 40 pg.

#### 4. RESULTS

In this study, two weathering clasts (AN-14-7.6 and AN-14-7.5) were characterized: both were oblate in shape. i.e., about 10 cm long, 7 cm wide, and 6 cm high and 15 cm long, 10 cm wide and 7 cm high, respectively (Fig. 3). The cores of both clasts are dark gray in color and are surrounded by  $\sim <1-3$  cm thick brownish-yellow weathering rinds. The core-rind boundary of both clasts is characterized with low to high values of curvature. Previous study has suggested that rind thickness increase with the curvature of the core-rind boundary (Sak et al., 2010). However, in this study, during removal of the clasts from the soil matrix, small portions of the outer rind corner disaggregated from the clasts and hence we do not observe a clear relationship between the rind thickness and the curvature. Major element contents for the core and rind samples from clast AN-14-7.6 and 7.5 are listed in Table 1: U and Th concentrations and U-series activity ratios are listed in Table 2.

#### 4.1. EMP observations

Quantitative XRD analysis indicates that the andesite bedrock sample collected from the bottom of the quarry consist of 68% plagioclase, 17% pyroxene, and 13% volcanic glass, with minor amounts (<1%) of vermiculite and minamiite/natroalunite inferred to be present due to hydrothermal alteration and weathering, respectively (Pereyra et al., 2016). The unweathered andesite core of clast AN-14-7.6 is porphyritic as observed in BSE images (Fig. 4a, b). The most abundant core material is fine groundmass and glass matrix (>60%). EMP spot analysis

Table 1
Major element (wt.%) and Zr contents (ppm) measured by ICP-OES for the unweathered bedrock and the core and rind materials of clast AN-14-7.6 and clast AN-14-7.5.

Samples	Type	Al <sub>2</sub> O <sub>3</sub> (%)	BaO (%)	CaO (%)	Fe <sub>2</sub> O <sub>3</sub> (%)	K <sub>2</sub> O (%)	MgO (%)	MnO (%)	Na <sub>2</sub> O (%)	P <sub>2</sub> O <sub>5</sub> (%)	SiO <sub>2</sub> (%)	SrO (%)	TiO <sub>2</sub> (%)	Zr (ppm)
Unweathered rock														
Bedrock 1	Quarry floor	16.30	0.02	6.35	7.62	1.38	2.64	0.14	3.21	0.11	59.70	0.03	0.74	98
Bedrock 2	Quarry side	16.80	0.02	6.98	7.48	1.30	3.04	0.17	3.26	0.11	59.10	0.03	0.71	99
Bedrock 3	Quarry floor	16.76	0.02	6.15	7.48	1.08	2.93	0.11	2.94	0.12	57.82	0.03	0.65	116
7.6 - La	Clast core	17.32	0.01	6.11	5.88	1.25	2.06	0.11	3.43	0.24	59.68	0.03	0.64	147
7.6 - Lb	Clast core	17.57	0.02	5.83	5.16	1.44	2.10	0.10	3.64	0.18	61.81	0.03	0.65	131
7.5 - L	Clast core	15.71	0.02	6.51	8.96	1.22	3.77	0.19	3.05	0.13	57.45	0.03	0.89	104
Clast 7.6 - Rind	Distance													
Low curvature (7.6L)	(mm)													
7.6 Lc	1	12.28	0.02	1.20	10.49	1.17	1.31	0.06	1.03	0.14	47.46	0.01	1.07	202
7.6 Ld	4.8	12.25	0.02	0.20	11.54	0.74	0.39	0.02	0.25	0.21	42.05	0.00	1.13	213
7.6 Le	7.5	11.35	0.01	0.14	12.50	0.09	0.30	0.02	0.15	0.19	37.60	0.00	1.11	209
7.6 Lf	11.5	12.65	0.01	0.21	11.23	0.04	0.28	0.01	0.16	0.14	38.79	0.00	1.15	217
7.6 Lg	15	12.44	0.00	0.17	13.60	0.03	0.26	0.01	0.15	0.17	36.60	0.00	1.19	228
Medium curvature (7.6	(M)													
7.6 Ma	1	9.72	0.02	0.49	10.72	0.92	0.86	0.04	0.58	0.17	39.91	0.00	1.13	195
7.6 Mb	5	8.79	0.01	0.15	10.96	0.26	0.30	0.01	0.21	0.17	35.98	0.00	1.02	198
7.6 Mc	9	9.85	0.00	0.23	11.63	0.09	0.31	0.01	0.20	0.26	37.69	0.00	1.08	234
7.6 Md	13	10.48	0.00	0.31	13.77	0.00	0.31	0.00	0.24	0.33	38.83	0.00	1.41	275
High curvature (7.6H)														
7.6 Ha	1	8.20	0.01	0.22	9.81	0.31	0.41	0.02	0.26	0.15	37.28	0.00	0.99	213
7.6 Hb	6	9.19	0.00	0.36	11.86	0.12	0.33	0.00	0.28	0.31	41.81	0.00	1.26	267
Clast 7.5 - Rind														
Low Curvature 1 (7.5).	L1)													
7.5 L1a	3	14.92	0.03	0.83	11.72	1.28	1.54	0.07	1.00	0.17	51.24	0.01	1.32	169
7.5 L1b	8	16.14	0.01	0.04	13.84	0.63	0.38	0.03	0.43	0.22	45.44	0.00	1.50	168
7.5 L1c	13	20.94	0.01	0.01	11.69	0.15	0.21	0.02	0.19	0.21	49.27	0.00	1.21	177
7.5 L1d	18	21.26	0.01	0.00	12.01	0.03	0.18	0.02	0.16	0.18	46.11	0.00	1.23	168
7.5 L1e	23	20.19	0.01	0.00	10.69	0.03	0.15	0.02	0.12	0.17	42.71	0.00	1.19	139
Low Curvature 2 (7.5).	L2)													
7.5 L2g	2	14.72	0.02	1.09	10.50	1.30	1.42	0.07	1.21	0.15	50.39	0.01	1.18	156
7.5 L2h	7	18.31	0.01	0.02	11.65	0.65	0.26	0.02	0.38	0.17	49.50	0.00	1.20	189
7.5 L2j	17	17.21	0.00	0.00	16.98	<.05	0.19	0.03	0.02	0.21	40.79	0.00	1.63	187
7.5 L2k	22	16.65	0.01	0.03	14.08	0.17	0.27	0.04	0.09	0.20	41.58	0.00	1.62	156

Table 2
U and Th contents (ppm) and U-series activity ratios measured by MC-ICPMS for the core and rind materials of clast AN-14-7.6 and clast AN-14-7.5.

Sample	Type	U (ppm)	+/-	$(^{234}U/^{238}U)$	+/-	Th (ppm)	+/-	( <sup>230</sup> Th/ <sup>232</sup> Th)	+/-	$(^{238}U/^{232}Th)$	+/-	$(^{230}Th/^{238}U)$	+/-
Unweathered rock													
7.6 core - La	Core	1.16	0.01	1.001	0.005	3.43	0.03	1.012	0.010	1.028	0.012	0.984	0.010
7.6 core - Lb	Core	1.12	0.01	1.005	0.005	3.34	0.03	1.019	0.010	1.025	0.012	0.995	0.010
7.5 core - L	Core	1.05	0.01	1.000	0.005	3.17	0.03	1.022	0.010	1.009	0.012	1.013	0.010
	Average $(N = 3)$	1.11	0.05	1.002	0.002	3.32	0.13	1.018	0.004	1.021	0.008	0.997	0.012
Clast 7.6 - Rind Low Curvature (7.6	Distance (mm)												
L)		1.75	0.02	1.002	0.005	4.67	0.05	1.055	0.011	1 142	0.014	0.022	0.000
7.6 Lc	1	1.75	0.02	1.003	0.005	4.67	0.05	1.055	0.011	1.143	0.014	0.923	0.009
7.6 Ld	4.8	1.96	0.02	1.008	0.005	4.83	0.05	1.076	0.011	1.241	0.015	0.867	0.009
7.6 Le	7.5	2.05	0.02	1.014	0.005	4.66	0.05	1.131	0.011	1.342	0.016	0.843	0.008
7.6 Lf	11.5	2.22	0.02	0.996	0.005	5.30	0.05	1.132	0.011	1.279	0.015	0.885	0.009
7.6 Lg	15	2.14	0.02	1.002	0.005	4.89	0.05	1.176	0.012	1.335	0.016	0.881	0.009
Medium Curvature (7	7.6 M)												
7.6 Ma	1	1.98	0.02	0.991	0.005	5.27	0.05	1.020	0.010	1.148	0.014	0.888	0.009
7.6 Mb	5	1.87	0.02	0.991	0.005	4.77	0.05	1.046	0.010	1.196	0.014	0.875	0.009
7.6 Mc	9	1.88	0.02	0.992	0.005	4.62	0.05	1.082	0.011	1.242	0.015	0.871	0.009
7.6 Md	13	2.44	0.02	1.013	0.005	5.37	0.05	1.187	0.012	1.390	0.017	0.854	0.009
High Curvature (7.6	H)												
7.6 Ha	1	2.06	0.02	0.989	0.005	5.39	0.05	1.027	0.010	1.165	0.014	0.882	0.009
7.6 Hb	6	2.20	0.02	0.989	0.005	5.40	0.05	1.059	0.011	1.244	0.015	0.851	0.009
7.6 Hc	10	2.50	0.02	0.998	0.005	5.71	0.06	1.090	0.011	1.336	0.016	0.815	0.008
Clast 7.5 – Rind													
Low Curvature 1 (7.5	(L1)												
7.5 La	3	1.60	0.02	0.991	0.005	4.16	0.04	1.046	0.010	1.177	0.012	0.889	0.009
7.5 Lb	8	1.88	0.02	0.987	0.005	5.07	0.05	1.081	0.011	1.136	0.011	0.952	0.010
7.5 Lc	13	1.71	0.02	0.986	0.005	4.47	0.04	1.099	0.011	1.167	0.012	0.941	0.009
7.5 Ld	18	1.47	0.01	0.983	0.005	3.75	0.04	1.119	0.011	1.198	0.012	0.934	0.009
7.5 Le	23	1.65	0.02	0.989	0.005	4.10	0.04	1.172	0.012	1.233	0.012	0.951	0.010
Low Curvature 2 (7.5	(L2)												
7.5 Lg	2	1.65	0.02	0.984	0.005	4.53	0.05	1.035	0.010	1.113	0.011	0.929	0.009
7.5 Lh	7	1.91	0.02	0.990	0.005	5.10	0.05	1.108	0.011	1.144	0.011	0.968	0.010
7.5 Lj	17	2.11	0.02	0.986	0.005	5.47	0.05	1.131	0.011	1.178	0.012	0.960	0.010
7.5 Lk	22	1.92	0.02	0.982	0.005	4.95	0.05	1.124	0.011	1.187	0.012	0.947	0.009
USGS basalt standard	d												
BCR2	Average $(N=3)$	1.70	0.02	1.003	0.003	5.88	0.05	0.881	0.002	0.884	0.006	0.996	0.010

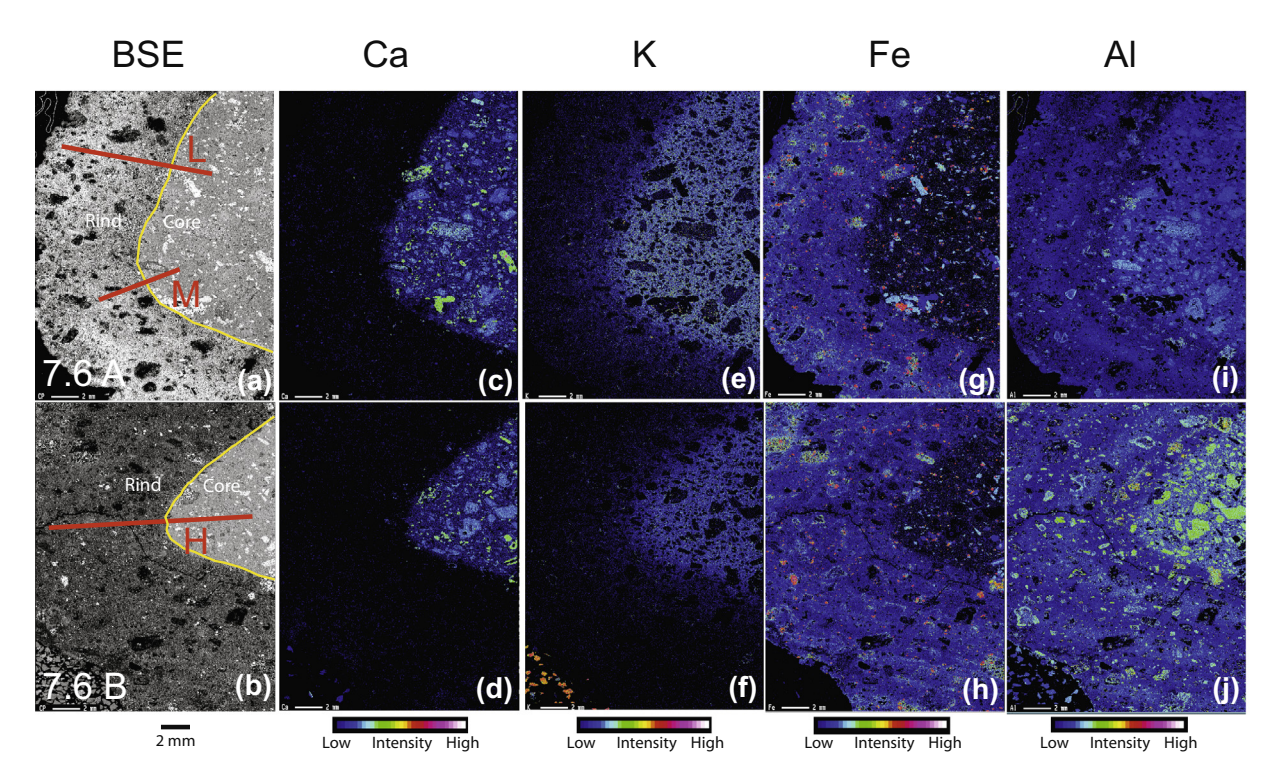


Fig. 4. (a) and (b) EMP backscatter images (BSE) of two thin sections (panel a and b) for clast AN-14-7.6. Yellow lines define the core-rind boundary and red lines (L, M, and H) indicate the locations of EMP element profiles for low, medium and high curvature sites. (c)–(j) X-ray element maps colored for the relative concentrations of elements: Ca, K, Fe, and Al. (For interpretation of the references to colour in this figure legend, the reader is referred to the web version of this article.)

indicates that the matrix material is predominantly  $\sim 60\%$  SiO<sub>2</sub>, 15% Al<sub>2</sub>O<sub>3</sub>, 10% Fe<sub>2</sub>O<sub>3</sub>, 2% K<sub>2</sub>O, 3% Na<sub>2</sub>O, 3% MgO and 4% CaO, present at andesitic composition. Phenocrysts (abundance <40%) in the core are generally plagioclase, pyroxene, or ilmenite, with grain sizes ranging from  $\sim 100$  to 2000 µm (Fig. 4). Plagioclase crystals were identified based on the observations of high contents of Ca, Na, Si on the EMP elemental maps (Fig. 4). Likewise, pyroxene was identified based on the observations of high Fe, Mg, and Si contents and ilmenite based on the Fe and Ti contents. The cores of the clasts studied here have similar chemical and mineralogical compositions to the core of the Bras David clast (Sak et al., 2010; Ma et al., 2012) and the local andesitic bedrock (Samper et al., 2007).

The rind material of clast AN-14-7.6 also shows fine-grained to porphyritic texture (Fig. 4a, b). EMP elemental maps indicate the fine rind material is significantly depleted in CaO and Na<sub>2</sub>O and relatively enriched in Fe<sub>2</sub>O<sub>3</sub> and TiO<sub>2</sub> compared to the core of the same clast (Fig. 4). Some phenocrysts were also observed in the rind, including ilmenite, highly altered pyroxene (SiO<sub>2</sub>- and Fe<sub>2</sub>O<sub>3</sub>-rich "ghost" crystals), and highly altered plagioclase (SiO<sub>2</sub>- and Al<sub>2</sub>O<sub>3</sub>-rich "ghost" crystals) (Fig. 4). We use the term "ghost" crystals to refer to pseudomorphic replacement of phenocrysts with secondary minerals.

Bulk chemistry along three profiles ( $\sim$ 25 mm-long), oriented approximately perpendicular to the high ( $\sim$ 0.43 mm<sup>-1</sup>), medium ( $\sim$ 0.16 mm<sup>-1</sup>), and low curvature ( $\sim$ 0.01 mm<sup>-1</sup>) core-rind boundary of clast AN-14-7.6, were

measured using EMP (Fig. 4a, b). Plots of EMP-measured wt.% K2O versus distance along the three EMP transects show depletion profiles in the rind (Fig. 5). As measured under EMP, the core has a relatively high but variable K<sub>2</sub>O content, ranging from 0.2 wt.% to 3.4 wt.%. Such variability in K<sub>2</sub>O content is expected when measured with EMP, given the large ( $\sim$ 100–2000 µm) phenocryst size and the small (20 µm) EMP spot size. The average wt.% K<sub>2</sub>O calculated for all the EMP point measurements in the core,  $1.7 \pm 1.2\%$ , consistent with the bulk composition measured by wet chemistry with OES (1.4 wt.%; Table 1). The rind-core boundary, shown as a line in Fig. 4, was the visually determined core-rind boundary on Fig. 3. Despite the large heterogeneity associated with the EMP point measurements, K<sub>2</sub>O concentrations show a clear decreasing trend from the core-rind boundary to the exterior of the rind for all three EMP profiles (Fig. 5).

Wt. % of CaO, Na<sub>2</sub>O, SiO<sub>2</sub>, and Al<sub>2</sub>O<sub>3</sub> also decrease similarly from the core to the rind (Appendix A). In contrast to the other oxides, the relative standard deviation of measurements of SiO<sub>2</sub> in the rind are larger than in the core. Finally, wt.% Fe<sub>2</sub>O<sub>3</sub> and TiO<sub>2</sub> increase gradually from the core to the rind and show relatively constant relative standard deviation across the entire transect (Appendix A).

These EMP observations (Fig. 4) are consistent with weathering of glass matrix, groundmass (fine crystals of plagioclase, pyroxene), and primary minerals (plagioclase, pyroxene) to Fe oxy-hydroxides, gibbsite and minor kaolinite.

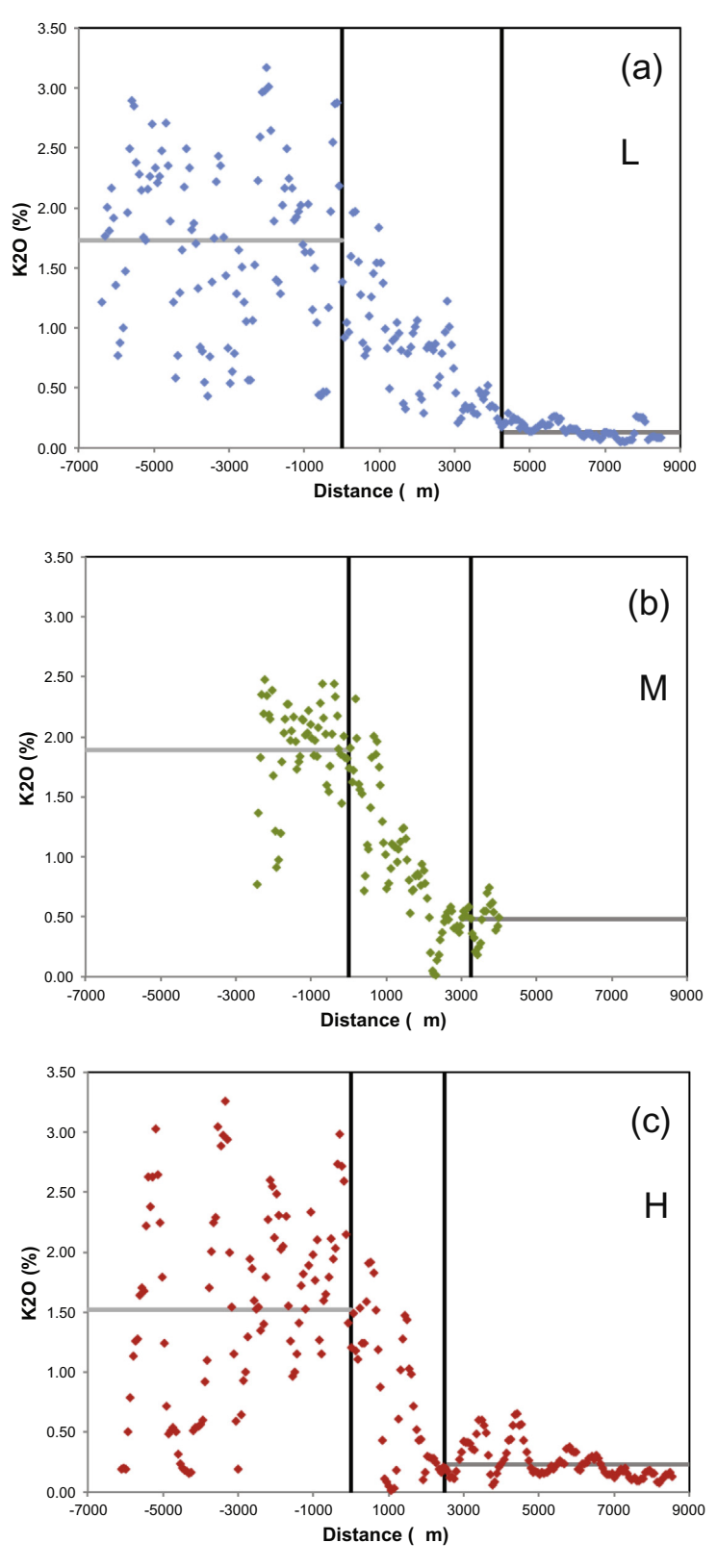


Fig. 5. EMP point measurements of  $K_2O$  contents (wt.%) for (a) low, (b) medium, and (c) high curvature transect (L, M, and H lines in Fig. 4) on clast AN-14-7.6. Horizontal gray lines indicate average values in core and rind point measurements, respectively. Vertical line at distance = 0 mm is visually defined core-rind boundary. Vertical line in the rind (distance > 0 mm) indicates visually defined reaction front for K (see text for details).

# 4.2. Major elements and open system mass transfer coefficients

Major element contents were also characterized by ICP-OES for bulk samples of core and rind material drilled on clasts AN-14-7.6 and AN-14-7.5. The major oxide contents in the core display little variability when measured on the cored samples of approximately 40 mm<sup>3</sup>, with compositions almost identical to the bulk composition of the unweathered bedrock material from depth in the quarry (Table 1). In contrast, compositions of the rind material are more variable, with the contents of Fe<sub>2</sub>O<sub>3</sub>, TiO<sub>2</sub>, and Zr generally increasing and CaO, Na<sub>2</sub>O, K<sub>2</sub>O, and MgO decreasing as a function of distance away from the core-rind boundary (Table 1).

To evaluate the loss or gain of major elements in a weathering rind (especially to correct for relative concentration changes due to changes of other elements in the rind), the open system mass transfer coefficient,  $\tau_{i,j}$  is often used. This parameter is calculated from concentrations (C) of a reference immobile element i and the element of interest (j) both in the weathered rind (w) and the parent material (p) (e.g., Brimhall and Dietrich, 1987; Anderson et al., 2002):

$$\tau_{i,j} = \frac{C_{j,w}}{C_{j,p}} \cdot \frac{C_{i,p}}{C_{i,w}} - 1. \tag{1}$$

A value of zero means that element j is as immobile in the altered material as the reference element i when compared to the parent material. Positive  $\tau_{i,j}$  values indicate the extent of enrichment of element j, and negative values define the fractional depletion of j with respect to the immobile element i compared to the parent (i.e. the fractional depletion  $= -\tau_{i,-j}$ ). A  $\tau_{i,-j}$  value of -1 indicates complete removal of the mobile element.

During weathering of andesite or basalt, Ti is often found to be relatively immobile as its major carrier phase in those lithologies (e.g. ilmenite) is close to insoluble (e.g., White et al., 1998; Sak et al., 2004, 2010; Neaman et al., 2006; Buss et al., 2008; Ma et al., 2012). In this study, ilmenite was observed in the BSE images of the studied clast (Fig. 3). Hence,  $\tau_{i,j}$  values for the weathering rind were calculated assuming Ti is the reference immobile element

For clasts AN-14-7.6 and AN-14-7.5, calculated  $\tau_{Ti,i}$  values for elements such as Ca, Na, and K decrease from 0.0 to almost -1.0 across the core-rind interface (Figs. 6 and 7). Such profiles are termed "completely developed" depletion profiles because ~100% of an element has become depleted (Brantley and White, 2009). The changes of  $\tau_{Ti,i}$  values for Ca, Na are abrupt across the core-rind interface, indicating nearly complete loss of these elements within a narrow alteration zone which we refer to as the reaction front (<2 mm as determined by bulk coring in Fig. 6, <3 mm as determined by EMP in Appendix A). The decrease of  $\tau_{Ti,j}$ values for K is more gradual (<7 mm as determined by bulk coring in Fig. 6, <5 mm as determined by EMP in Fig. 5). The more gradual change across the K reaction front documents that the loss of K is slower than the loss of Ca and Na.

The  $\tau_{Ti,j}$  values for Si and Al all decrease gradually from 0.0 in the core to values between -0.5 and -0.9 in the rind, showing incompletely developed depletion profiles (Si shown in Figs. 6 and 7). For elements that show either completely developed (Ca, Na, K) or incompletely developed (Si, Al) depletion profiles in the rind, the extents of depletion all systematically decrease with curvature of the corerind boundary when comparing sites equidistant from the core-rind boundary (Figs. 6 and 7).

Calculated  $\tau_{Ti,j}$  values for Zr and Fe remain relatively close to 0 across the rind (Figs. 6 and 7), indicating that Zr and Fe are mostly immobile (Brantley and White, 2009). The rind for AN-14-7.6 shows slightly positive  $\tau_{Ti,Fe}$  values between 0.1 and 0.3 that may define an addition profile (Fig. 6f). However, the  $\tau_{Ti,Fe}$  values for AN-14-7.5 show an immobile profile. The slightly positive  $\tau_{Ti,Fe}$  values in AN-14-7.6 may be due to some local heterogeneity in the core at the clast scale.

# 4.3. U and Th concentrations and activity ratios

Average U and Th concentrations of all drilled core samples of AN-14-7.6 and AN-14-7.5 are  $1.11\pm0.05$  ppm and  $3.32\pm0.13$  ppm, respectively (Table 2). Rind samples of AN-14-7.6 and AN-14-7.5 have higher U and Th concentrations than the core samples, ranging from 1.60 ppm to 2.50 ppm for U and 3.75 ppm to 5.71 ppm for Th (Table 2).

U-series activity ratios of drilled core samples for both clasts show very limited variations (Table 2), as expected for a homogenous core. The average for ( $^{234}\text{U}/^{238}\text{U}$ ) and ( $^{230}\text{Th}/^{238}\text{U}$ ), where the parentheses indicate activity ratios, are  $1.002 \pm 0.002$  and  $0.997 \pm 0.012$ , respectively (Table 2). These values are close to secular equilibrium within errors, as expected for the 1.7 Ma basaltic andesite bedrock. In other words, given the half life of  $^{234}\text{U}$  and  $^{230}\text{Th}$  for the U-series system, the core sample U and Th have decayed to secular equilibrium in the 1.7 Ma since emplacement. Measured ( $^{234}\text{U}/^{238}\text{U}$ ) and ( $^{230}\text{Th}/^{238}\text{U}$ ) activity ratios of the rind samples of both clasts range from  $0.982 \pm 0.005$  to  $1.014 \pm 0.005$  and from  $0.815 \pm 0.010$  to  $0.968 \pm 0.010$ , respectively, significantly different from the core samples.

Measured ( $^{238}$ U/ $^{232}$ Th) activity ratios of these rind samples on both clasts range from 1.113  $\pm$  0.010 to 1.390  $\pm$  0.010 and ( $^{230}$ Th/ $^{232}$ Th) activity ratios range from 1.020  $\pm$  0.010 to 1.187  $\pm$  0.010, also higher than the core samples (Table 2). More importantly, ( $^{238}$ U/ $^{232}$ Th) and ( $^{230}$ Th/ $^{232}$ Th) activity ratios of the five core-rind transects all increase continuously and systematically with distance from core to rind (Figs. 8 and 9).

# 5. DISCUSSION

# 5.1. Sequences of weathering reactions during rind formation

During rind formation, the extent of elemental loss, based on the  $\tau_{Ti,j}$  values in the rinds from both clasts in this study decreases in the order  $Ca \approx Na > K \approx Mg > Si \approx Al > Zr \approx Ti \approx Fe$  (Figs. 6 and 7). The order of element depletion is consistent with the sequence of weathering

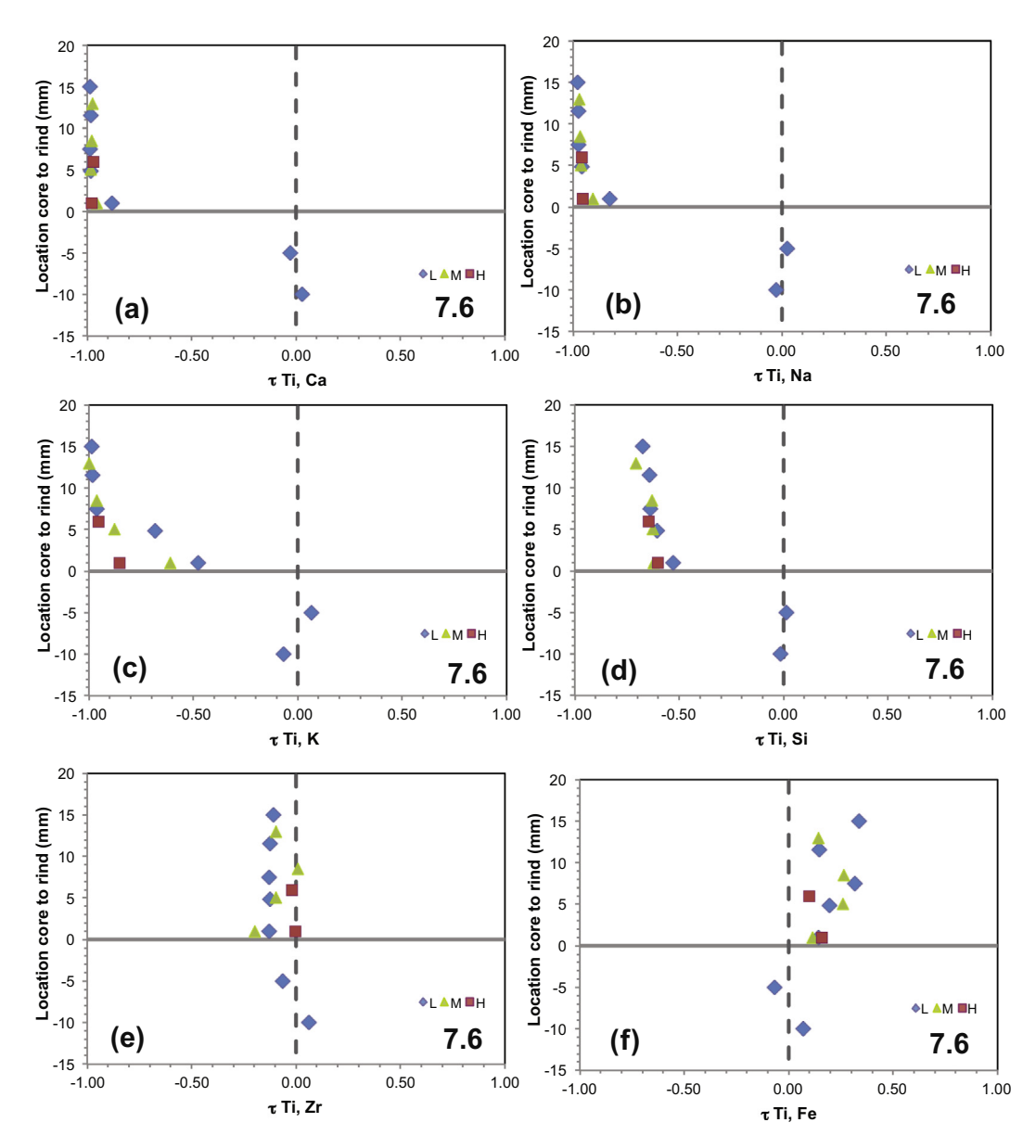


Fig. 6. Elemental mass transfer coefficients  $\tau_{Ti,j}$ : (a) Ca, (b) Na, (c) K, (d) Si, (e) Zr and (f) Fe, calculated using Eq. (1) plotted as a function of position relative to the core–rind boundary (indicated as position 0) for the low, medium, and high curvature transect on clast AN-14-7.6. The core–rind interface was defined following the same method in Sak et al. (2010). Values of  $\tau_{Ti,j}$  are estimated to vary by  $\sim$ 9% as shown in the representative error bar due to variations in Ti and major element measurements and parent heterogeneity.

reactions starting at the rind-core boundary including weathering of plagioclase, pyroxene in both groundmass matrix and phenocrysts, and glass matrix. Similar sequences of weathering reactions have been observed in the weathering clast previously studied for the Bras David watershed (Sak et al., 2010; Ma et al., 2012). For example, the nearly complete loss of Ca and Na is attributed to rapid weathering of glass matrix and. Indeed, the EMP X-ray elemental maps show that groundmass material and phenocrysts of plagioclase weathered rapidly across the corerind boundary in clast AN-14-7.6 (Fig. 4; Appendix A). In contrast, weathering of pyroxene and glass matrix accounts for the more gradual depletion of Mg and K (Fig. 4). The gradual depletion of K during weathering

reactions (Figs. 5–7) documents that the major K-containing mineral(s) such as glass matrix is largely depleted but that some secondary minerals (such as kaolinite, Sak et al., 2010) retain K in the rind in the early stage of weathering. The formation of gibbsite, Fe and Al oxyhydroxides, and kaolinite are consistent with the observed retention of Si, Al, and Fe in the rind of clast AN-14-7.6 (Fig. 4). The conservative behavior of Ti, Zr, and Fe (Figs. 6 and 7) is consistent with observations of immobility during weathering of other basaltic rocks (e.g. Neaman et al., 2006). For example, ilmenite is a major carrier phase for Ti in basaltic rocks and usually stable during chemical weathering. Indeed, both Ti and Fe show increasing concentrations from the core to the rind on the EMP profiles,

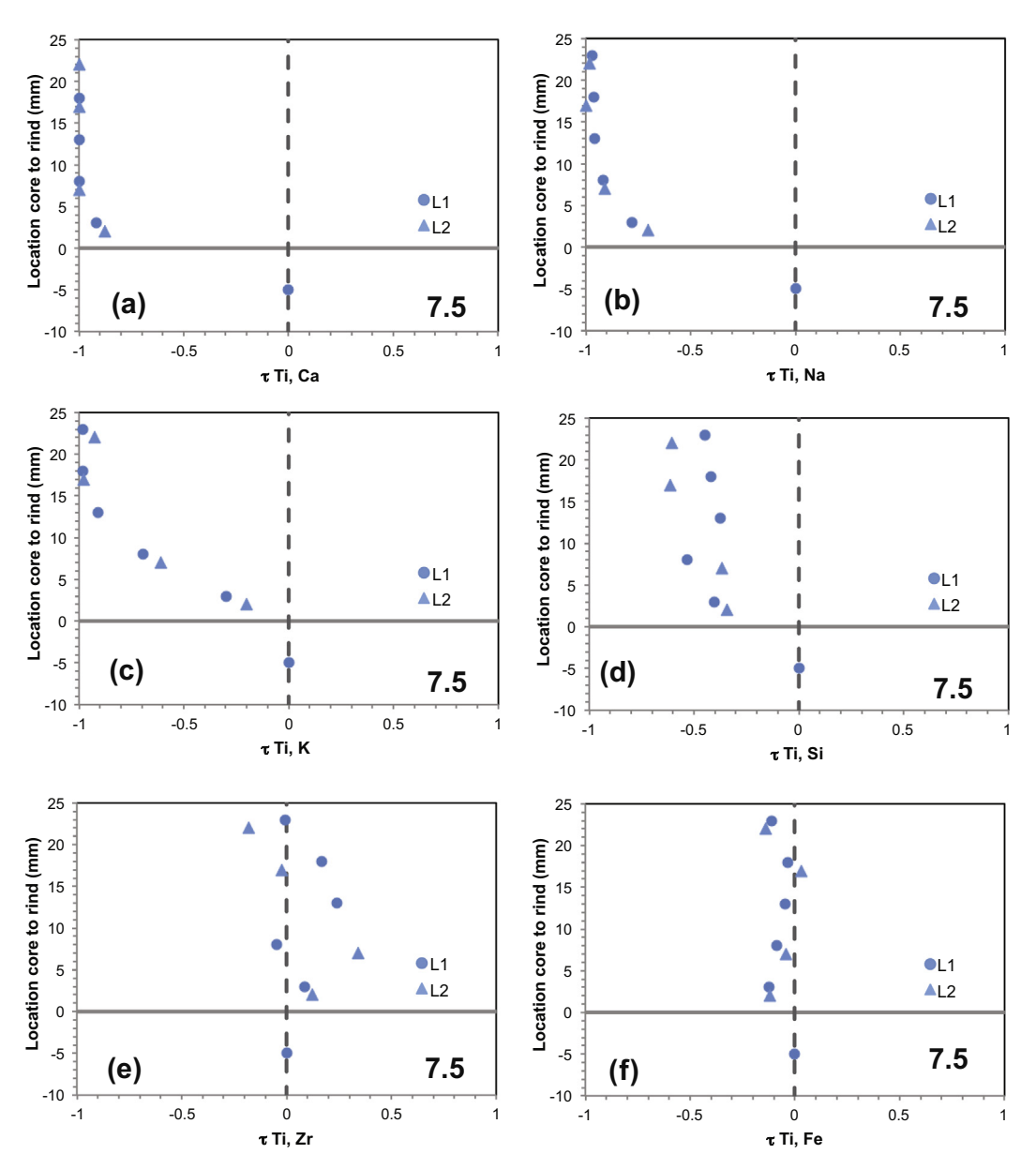


Fig. 7. Elemental mass transfer coefficients  $\tau_{\text{Ti,j}}$ : (a) Ca, (b) Na, (c) K, (d) Si, (e) Zr and (f) Fe, calculated using Eq. (1) plotted as a function of position relative to the core–rind boundary (indicated as position 0) for the two transects on clast AN-14-7.5. The core–rind interface was defined following the same method in Sak et al. (2010). Values of  $\tau_{\text{Ti,j}}$  are estimated to vary by ~9% as shown in the representative error bar due to variations in Ti and major element measurements and parent heterogeneity.

consistent with their immobile behavior during rind formation (Appendix A).

# 5.2. Variations of reaction front thickness with reaction constant and curvature

During rind formation, water-rock interactions create a transition zone (reaction front) across which primary minerals dissolve or secondary minerals form (Brantley and White, 2009). Previous modeling explored the factors controlling reaction front thickness in porous water-mineral systems (Lichtner, 1988; Lebedeva et al., 2007, 2010, 2015; Brantley and White, 2009; Navarre-Sitchler et al.,

2011; Reeves and Rothman, 2014). In these models, solute can be transported either by advection or diffusion: the rinds at the low-porosity rind-core boundary such as near the andesite core studied here are assumed to be diffusion controlled. In the high porosity outer part of the rind, the transport can be advection controlled. In a single component water–mineral system treated as a one-dimensional system where solute transport is dominantly by diffusion, the reaction front thickness (h) for a given reaction occurring in a rock is proportional to:

$$h \propto \left(\frac{\phi D}{kA}\right)^{1/2} \tag{2}$$

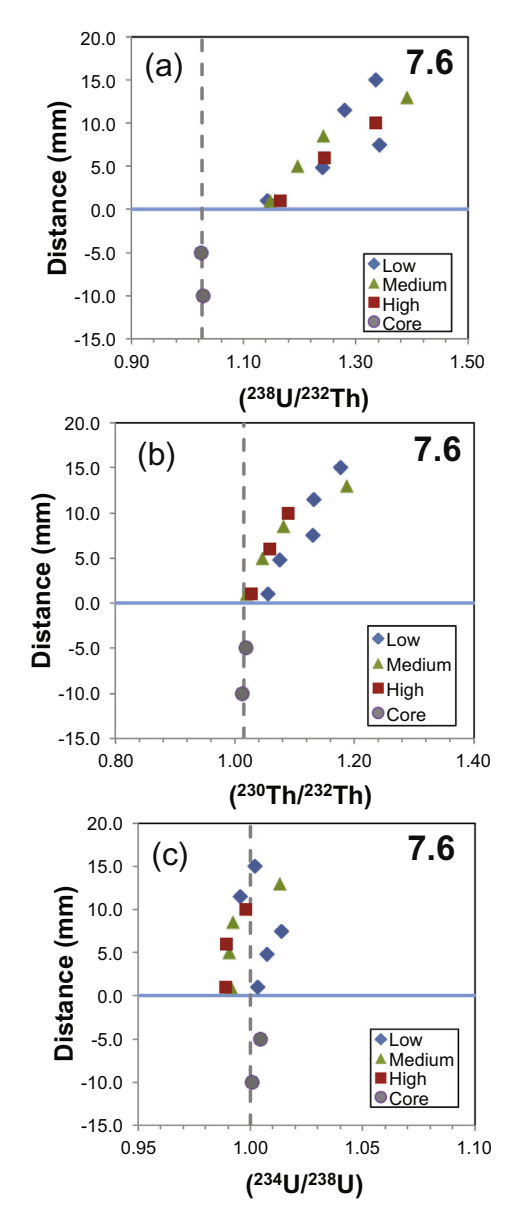


Fig. 8. Measured U–Th activity ratios, (a)  $(^{238}\text{U}/^{232}\text{Th})_a$ ; (b)  $(^{230}\text{Th}/^{232}\text{Th})_a$ ; (c)  $(^{234}\text{U}/^{238}\text{U})_a$  plotted as a function of position relative to the core–rind boundary for the low, medium, and high curvature site on clast AN-14-7.6. Grey circles indicate measured core activity ratios (Table 2). Error bars in  $(^{238}\text{U}/^{232}\text{Th})$ ,  $(^{230}\text{Th}/^{232}\text{Th})$ , and  $(^{234}\text{U}/^{238}\text{U})$  activity ratios are smaller than the size of symbols.

where  $\phi$  is porosity of the weathering material, D is the diffusivity of solutes through the porous material (cm<sup>2</sup> s<sup>-1</sup>), k is the reaction rate constant (mol cm<sup>-2</sup> s<sup>-1</sup>) and A is the mineral-water interfacial area (cm<sup>2</sup>) (Lichtner, 1988).

In this study, the thickness of the reaction front can be inferred from elemental depletion profiles across the corerind boundary for both clasts. For example, Ca and Na are completely depleted within ~2 mm distance from the rind-core boundary on clast AN-14-7.6, i.e., the reaction front thickness for Ca and Na is 2 mm (Fig. 6a, b). In contrast, K shows a wider reaction front with complete

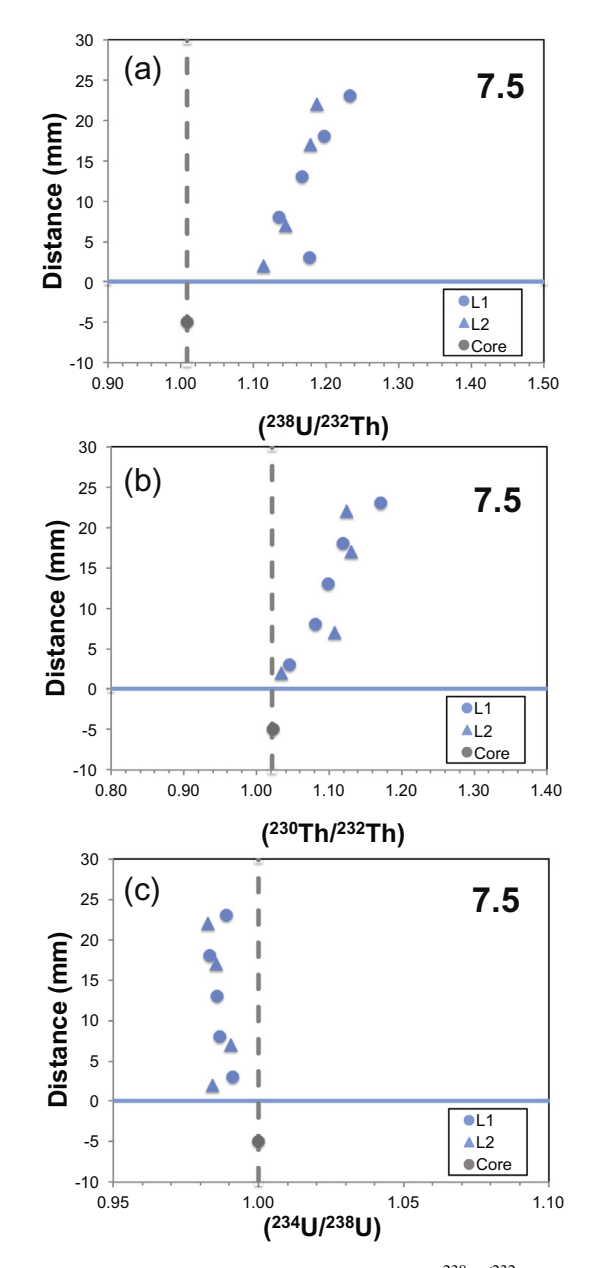


Fig. 9. Measured U–Th activity ratios, (a)  $(^{238}\text{U}/^{232}\text{Th})_a$ ; (b)  $(^{230}\text{Th}/^{232}\text{Th})_a$ ; (c)  $(^{234}\text{U}/^{238}\text{U})_a$  plotted as a function of position relative to the core–rind boundary for the two low curvature sites on clast AN-14-7.5. Grey circles indicate measured core activity ratios (Table 2). Error bars in  $(^{238}\text{U}/^{232}\text{Th})$ ,  $(^{230}\text{Th}/^{232}\text{Th})$ , and  $(^{234}\text{U}/^{238}\text{U})$  activity ratios are smaller than the size of symbols.

depletion occurring at  $\sim$ 6 mm to  $\sim$ 13 mm distance from the rind-core boundary (Fig. 6c). Si shows an even wider reaction front than K (Fig. 6d). For locations on the clast with the same curvature, the observed reaction front thickness (h) always increases from Ca (and Na) to K to Si on AN-14-7.6 (Fig. 6) and AN-14-7.5 (Fig. 7). In a single component water—mineral system, both the porosity ( $\phi$ ) and the diffusivity of solutes (D) are largely controlled by the properties of porous media (e.g. Navarre-Sitchler et al., 2009). The diffusivity (D) can vary between solutes but such variation for Ca, Na, K, and Si is assumed to be

minor (e.g., White, 2014). We therefore assume these values are the same for each element. Hence, the increasing h values are attributed to a decrease in the apparent dissolution rate constant (kA) from Ca (and Na) to K and Si, as evidenced by rapid weathering of groundmass matrix and plagioclase for release of Ca and Na compared to slow release of K and Si from groundmass and glass matrix. Unlike Ca and Na that are completely depleted due to dissolution during andesite weathering, both Si and K involve both dissolution and precipitation (or retention by secondary minerals) during rind formation. The wider reaction fronts for Si and K are consistent with the re-precipitation or retention events that are inferred to occur in the rind.

The thickness of the reaction fronts documented by depletion of Ca. Na. and K correlated inversely with curvature on clast AN-14-7.6. For example, the high-curvature transect always shows the narrowest reaction front, and the low-curvature transect has the widest reaction front (Fig. 6). The high-resolution EMP profiles on clast AN-14-7.6 reveal the same trend: the thickness of the K reaction front is observed to equal  $\sim 2500 \,\mu\text{m}$ ,  $\sim 3250 \,\mu\text{m}$ , and  $\sim$ 4250 µm in the high-, medium-, and low-curvature transects, respectively (Fig. 5). Here, we estimated the reaction front thickness as the distance over which the EMP K<sub>2</sub>O% concentrations decrease from the average value in the core to the average value in the outer rind. Such an observation however cannot be interpreted directly from Eq. (2) because the equation was derived from a 1D that did not include curvature. Recently, Lebedeva et al. (2015) expanded the 1D model to a 2D multi-mineral reactive-diffusion model. That study explored the effects of curvature on weathering and has predicted two important hypotheses: (1) weathering rate of a rind on a clast (advancing rate of the reaction front) correlates positively with porosity  $(\phi)$ , diffusivity (D), and curvature (K); and (2) the reaction front thickness hincreases with curvature K. Lebedeva et al. derived the following equation:

 $h = D\phi K/(kA)$ 

(Eq. (17) in Lebedeva et al., 2015). The equation contradicts our observations that the front thickness decreases with increasing curvature. We currently have no satisfactory explanation for that observation. It is noted that the reactive-diffusion model assumes an isotropic material for reactions (e.g. Lebedeva et al., 2015). If the core or the rind materials have anisotropic structures at small scales that may lead to different diffusivity or effective porosity from an isotropic case, this may explain the contradictions in the front thickness. Unfortunately we do not have any direct evidence to test this specific hypothesis now.

In the following sections, we will discuss how U-series disequilibria in weathering rinds help to explore the prediction that weathering advance rate is positively correlated with curvature at the clast scale and also to investigate the control of precipitation in watersheds on weathering advancing rates in rinds.

5.2.1.  $^{238}U^{-234}U^{-230}Th$  disequilibria in weathering rind

Processes during rind formation have modified the U-series activity ratios such as (238U/232Th), (234U/238U)

and (<sup>230</sup>Th/<sup>232</sup>Th) in the rind and the resulting <sup>238</sup>U-<sup>234</sup>U-<sup>230</sup>Th disequilibria have been used to determine rind formation ages and weathering rates (e.g., Pelt et al., 2008; Ma et al., 2012).

The U-series disequilibria result from the fact that trace elements U and Th display different mobility during chemical weathering and rind formation (e.g., Chabaux et al., 2003a). Th is generally immobile and particle-reactive during water-rock interaction due to its extremely low solubility in water (e.g., Rosholt et al., 1966; Latham and Schwarcz, 1987a.b; Gascovne, 1992; Chabaux et al., 2003a). Indeed, conservative behavior of Th has been commonly observed in tropical soils, saprolite, and weathering rinds in Cameroon, China, Costa Rica, and Guadeloupe (Braun et al., 1993; Ma et al., 2007, 2012; Pelt et al., 2008). Unlike Th, U is mobile during water-rock interactions under oxidizing conditions (e.g., Chabaux et al., 2003a). U immobilization occurs when the environmental conditions change to reducing conditions, where solubilities of U-containing phases are much lower (Chabaux et al., 2003a, 2008 and references therein). U fixation also occurs due to co-precipitation or sorption of U onto newly formed secondary Fe-hydroxides (Ames et al., 1983; Shirvington, 1983; Andersson et al., 1998; Duff et al., 2002; Chabaux et al., 2003a, 2008 and references therein).

(238U/232Th) activity ratios of the five rind transects on clast AN-14-7.6 and clast AN-14-7.5 all increase almost linearly with increasing distance from the rind-core boundary (Figs. 8a, 9a). This increase provides evidence of a continuous addition of U during rind formation if Th is immobile. Comparing Th concentrations with other immobile elements such as Ti and Zr can justify such an assumption. For example, in both clast AN-14-7.5 and AN-14-7.6, the Th/Zr and Th/Ti ratios of the rinds show similar ranges of variations with the Th/Zr and Th/Ti ratios in the respective cores (Appendix B), documenting the immobile behavior of Th, Ti, and Zr. It is noted that the relatively large variations of Th/Zr and Th/Ti ratios (especially in clast AN-14-7.6) probably due to the associated uncertainties of two different types of analytical methods (e.g. Th was measured by the isotope dilution method with MC-ICP-MS on one set of samples while Ti and Zr were measured on ICP-OES on a separate set of drilled samples). For this reason, we do not further discuss the mobility behavior of U with respect to Ti, but instead use Th as the immobile reference element for the U-series data.

Soil pore water is most likely the source of external U to the rind. U can be carried as a solute in such oxidizing weathering environments (e.g., Chabaux et al., 2003a). Given that the outer rind minerals are highly oxidized (e.g. contain Fe oxy-hydroxides) and the unweathered core minerals are reduced (presence of pyroxene, ilmenite), it is possible that the activity of oxygen in soil pore water decreases with infiltration inward to the rind-core boundary, generating a reducing condition for the dissolved U in the infiltration soil pore water to start to precipitate near the core-rind boundary. However, the (238U/232Th) ratio linearly increases with distance away from the core-rind boundary for all five transects on both clasts (Figs. 8 and 9). We therefore argue that U is added from the core-rind

boundary to the rind continuously at a nearly constant rate. Such a continuous U fixation could be attributed to coprecipitation or sorption of U onto secondary Fehydroxides in the rind as soil pore water infiltrates through the rind continuously with abundant Fehydroxides. Similar U addition in weathering products, due to both changes of redox conditions and/or absorption onto Fehydroxides, have also been documented in soil profiles (Dequincey et al., 2002; Chabaux et al., 2003b; Dosseto et al., 2008b; Ma et al., 2010), in river sediments (Andersson et al., 1998; Dosseto et al., 2006; Granet et al., 2007, 2010), and in weathering basaltic clasts previously studied in Costa Rica (Pelt et al., 2008) and Guadeloupe (Ma et al., 2012).

U is soluble in water and <sup>234</sup>U is released to solution to greater extent than <sup>238</sup>U (Fleischer, 1980). <sup>234</sup>U is thought to be released preferentially, because it is produced by alpha particle emission from <sup>238</sup>U decay that damages the crystal lattice (Fleischer, 1980). For these reasons, fluid phases are generally characterized by (<sup>234</sup>U/<sup>238</sup>U) activity ratios >1 while residual solid materials that have recently been weathered are generally characterized by (<sup>234</sup>U/<sup>238</sup>U) activity ratios <1 (e.g., Rosholt et al., 1966; Vigier et al., 2001; Chabaux et al., 2003a, 2008; Dosseto et al., 2008a; Andersen et al., 2009). The observed (234U/238U) values of the rind samples in both clasts range from 0.982 to 1.014, consistent with two important processes during rind formation: (1) chemical leaching that generates (<sup>234</sup>U/<sup>238</sup>U) ratios <1 in the solid weathering products; and (2) continuous addition of U as a precipitate or sorbate from soil pore waters with  $(^{234}\text{U}/^{238}\text{U})$  ratios >1, which results in excess  $^{238}\text{U}$  and  $^{234}\text{U}$  in the rind materials. Both U addition and leaching processes during chemical weathering modify the  $(^{234}\text{U}/^{238}\text{U})$  activity ratios in the rind. Over time, the excess  $^{234}$ U (half-life,  $T_{1/2} = 244$  kyr) decays to  $^{230}$ Th ( $T_{1/2} = 75$  kyr) that in turn modifies ( $^{234}$ U) $^{238}$ U) ratios in the rind. Hence, the  $(^{234}\text{U}/^{238}\text{U})$  values of the rind samples are more variable with respect to distance from the corerind boundary (Figs. 8c, 9c). By contrast, the subsequent radioactive production of <sup>230</sup>Th and the immobile behavior of Th isotopes account for the observed continuous increase of (230Th/232Th) activity ratios for all five rind profiles (Figs. 8b and 9b).

# 5.3. Rind formation ages and weathering rates calculated with $^{238}\mathrm{U}\text{-}^{234}\mathrm{U}\text{-}^{230}\mathrm{Th}$ disequilibria

With an open-system U-series mass balance model that allows for continuous chemical leaching and addition of U-series isotopes during rind formation (Dequincey et al., 2002; Ma et al., 2012 and references therein), the changes of U-series isotopes with time in the rind can be modeled as:

$$\frac{d^{238}U}{dt} = f_{238} - \lambda_{238}^{238}U - k_{238}^{238}U$$
 (3)

$$\frac{d^{234}U}{dt} = f_{234} + \lambda_{238}^{238}U - \lambda_{234}^{234}U - k_{234}^{234}U$$
 (4)

$$\frac{d^{230}\text{Th}}{dt} = \lambda_{234}^{234}\text{U} - \lambda_{230}^{230}\text{Th}$$
 (5)

$$\frac{d^{232}\text{Th}}{dt} = -\lambda_{232}^{232}\text{Th} \tag{6}$$

Here, <sup>238</sup>U, <sup>234</sup>U, <sup>230</sup>Th, and <sup>232</sup>Th are the concentration terms (atoms g<sup>-1</sup>) in the rind; terms  $\lambda_{238}$ ,  $\lambda_{234}$ ,  $\lambda_{230}$ , and  $\lambda_{232}$  are the decay constants for <sup>238</sup>U, <sup>234</sup>U, <sup>230</sup>Th and <sup>232</sup>Th (yr<sup>-1</sup>);  $f_{238}$  and  $f_{234}$  are the addition rates of <sup>238</sup>U and <sup>234</sup>U into the rind (atoms g<sup>-1</sup> yr<sup>-1</sup>). The f terms lump together all the processes that add U isotopes into the rind material such as precipitation and adsorption of U from soil water, separate from radioactive production. The f terms are assumed to be constant with time for the purpose of simplicity and tractability of the model (Ghaleb et al., 1990; Dequincev et al., 2002; Ma et al., 2012). The closeto-linear increase of (<sup>238</sup>U/<sup>232</sup>Th) ratios with distance from the core into the rinds along the five analyzed transects (Figs. 8a, 9a) is consistent with the assumption of constant U input rate (f terms) in the model. The terms  $k_{238}$  and  $k_{234}$ are first-order rate constants (yr<sup>-1</sup>) for chemical leaching of <sup>238</sup>U and <sup>234</sup>U from U-containing phases (Latham and Schwarcz, 1987a,b; Plater et al., 1992; Vigier et al., 2001), i.e. the U release rates equal  $k_{238}^{238}$ U and  $k_{234}^{234}$ U. For a given rind sample, t is the rind formation age (in years). Explicitly, rind formation starts when the water-mineral interfacial area at the core-rind boundary becomes large enough to facilitate mobilization/immobilization of U-series isotopes during weathering reactions. Here, we assume the visually defined core-rind boundary as the starting point of weathering (t = 0) and the rind formation ages increase with the position from the core-rind boundary into the rind. The combined term,  $(\lambda_{234}f_{234})/(\lambda_{238}f_{238})$ , represents the  $(^{234}\text{U}/^{238}\text{U})$  activity ratio of the input source, e.g., the infiltrating soil water. The term,  $k_{234}^{234}\text{U}/k_{238}^{238}\text{U}$  describes ratio between the release rate of  $^{234}\text{U}$  due to phenomena related to alpha particle damage to the crystal lattice  $(k_{234})$  and the release rate due to dissolution of the mineral

For rind samples on each rind transect (L, M. H on AN-14-7.6 and L1 and L2 on AN-14-7.5), measured (238 U/232 Th), (230 Th/232 Th), and (234 U/238 U) activity ratios were used as input values to solve unknown parameters (f<sub>238</sub>, f<sub>234</sub>, k<sub>238</sub>, k<sub>234</sub>, and individual t) with an inverse Monte-Carlo algorithm (Appendix C and D). The core U-series compositions were sued as the initial composition in the model. The model calculations show both (238 U/232 Th) and (230 Th/232 Th) ratios increase with rind formation ages (Figs. 10 and 11; Table 3), consistent with the measured ratios in rind samples for each profile. Furthermore, the rind formation ages for all five transects generally increase with distance away from the core-rind boundary, consistent with the order of rind formation (Fig. 12).

Model-derived  $k_{238U}$  values from the five rind profiles vary from  $1.1 \times 10^{-5}$  to  $1.6 \times 10^{-5}$  yr<sup>-1</sup> (Table 3), within the range of <sup>238</sup>U rate constants derived from weathering profiles or river sediments with similar weathering time scales (Dosseto et al., 2008a; Ma et al., 2010, 2013). Similarly, model-derived  $k_{234}/k_{238}$  ratios are all greater than one, varying from 1.1 to 1.4 (Table 3), consistent with the fact that <sup>234</sup>U isotope is preferentially lost to the weathering fluids compared to <sup>238</sup>U (e.g., Fleischer, 1980). Such a range of values agrees well with many field and experimental studies of U isotopic fractionation during water–rock

1.00

0.90

1.00

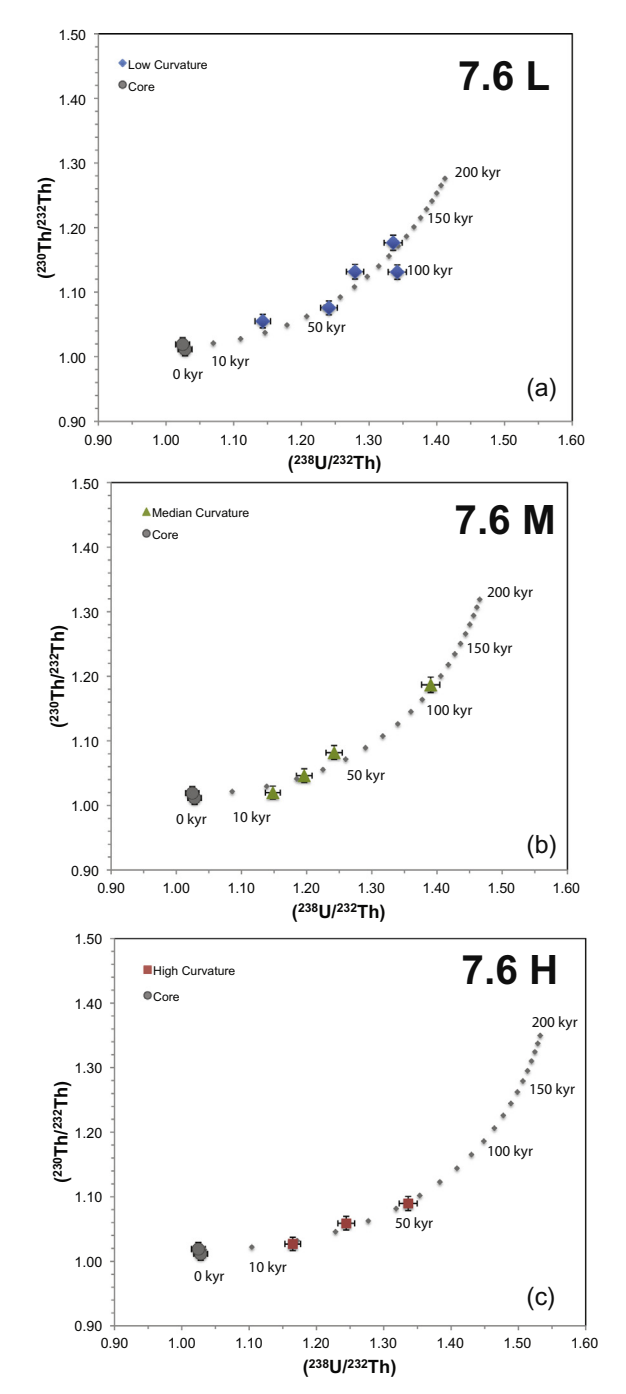


Fig. 10.  $(^{230}\text{Th}/^{232}\text{Th})_a$  vs.  $(^{238}\text{U}/^{232}\text{Th})_a$  isochron diagram for (a) low, (b) medium, and (c) high curvature transect on clast AN-14-7.6. The analytical error bars are within the symbol size. Two core samples are at secular equilibrium. The U–Th radioactive disequilibrium of the weathering rind samples from all three transects is explained by (1) continuous input of U plus leaching of U starting at the core–rind boundary (without addition or loss of Th), and (2) subsequent production of  $^{230}\text{Th}$  from U-series decay series in the rind. Rind formation ages were determined by an open-system U addition model (see text and Appendix C for details). When the model is solved (Table 3), the activity ratios of  $(^{238}\text{U}/^{232}\text{Th})$  and  $(^{230}\text{Th}/^{232}\text{Th})$  are calculated as a function of rind formation ages and are shown as the gray dots.

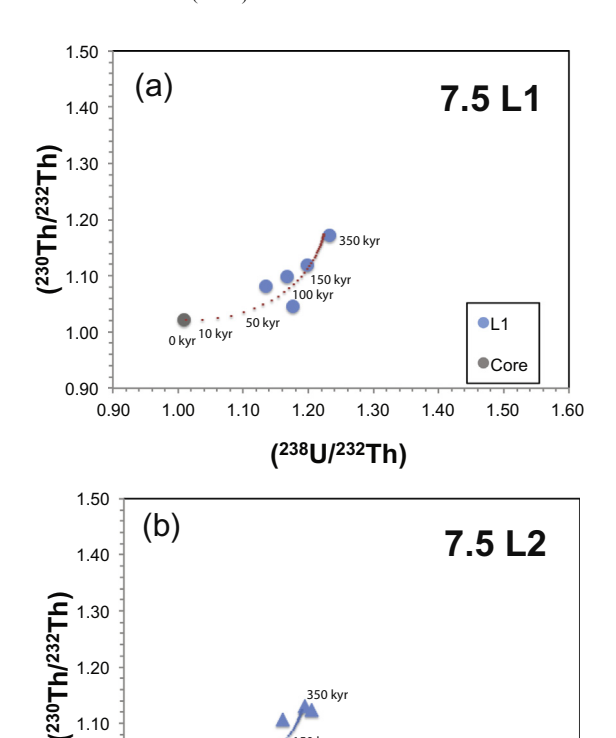


Fig. 11.  $(^{230}\text{Th}/^{232}\text{Th})_a$  vs.  $(^{238}\text{U}/^{232}\text{Th})_a$  isochron diagram for the two low curvature transects on clast AN-14-7.5. The analytical error bars are within the symbol size. The core sample is at secular equilibrium. Rind formation ages were determined by an open-system U addition model (see text and Appendix C for details). When the model is solved (Table 3), the activity ratios of  $(^{238}\text{U}/^{232}\text{Th})$  and  $(^{230}\text{Th}/^{232}\text{Th})$  are calculated as a function of rind formation ages and are shown as the gray dots.

1.20

(238U/232Th)

▲L2

1.50

1.60

interaction (e.g., Vigier et al., 2001; Dequincey et al., 2002; Dosseto et al., 2008b; Andersen et al., 2009). Model results also indicate that the rind experienced addition of U with f values ranging from  $1.5 \times 10^{-5}$  to  $2.5 \times 10^{-5}$  yr<sup>-1</sup>. The f values are in general greater than the k values (Table 3), indicating net addition of U to the rind due to the dual processes of U mobility. The model derived  $f_{234}/f_{238}$  ratios are also greater than one (1.03 –1.33), consistent with U addition from the infiltrating soil water. For each profile, the derived  $f_{234}/f_{238}$  value is similar to the derived  $k_{234}/k_{238}$  value. An implication of this is that the dual processes of U mobility could lead to either increases of  $(^{234}\text{U}/^{238}\text{U})$   $(f_{234}/f_{238} > k_{234}/k_{238})$  or decrease of  $(^{234}\text{U}/^{238}\text{U})$   $(f_{234}/f_{238} < k_{234}/k_{238})$  with time (Dequincey et al., 2002), consistent with the observed non-linear changes of  $(^{234}U/^{238}U)$  ratios in the rinds (Figs. 8c and 9c).

It is expected that the outermost rind should have the same weathering age as the total weathering age of the clast if little to no material has been eroded and lost to the

Table 3
Rind formation ages, advance rates, and model parameters determined from U-series disequilibria.

Sample	Distance (mm)	Age (kyr)		Weathering advance rate (mm/kyr)	$R^2$
7.6 L				$0.11 \pm 0.04$	0.74
7.6 Lc	1	$30.1 \pm 7.9$			
7.6 Ld	4.8	$60.9 \pm 11.7$			
7.6 Le	7.5	$102.6 \pm 11.1$			
7.6 Lf	11.5	$85.3 \pm 10.5$			
7.6 Lg	15	$117.5 \pm 9.6$			
$f_{238}/^{238}U_0 (yr^{-1})$	$F^{234}U/F^{238}U$	$k^{238}U (yr^{-1})$	$k^{234}U/k^{238}U$		
$1.54 \pm 0.75 \times 10^{-5}$	$\boldsymbol{1.19 \pm 0.13}$	$1.08 \pm 0.61 \times 10^{-5}$	$1.22 \pm 0.18$		
7.6 M				$0.12\pm0.05$	0.85
7.6 Ma	1	$21.9 \pm 6.7$			
7.6 Mb	5	$33.4 \pm 8.8$			
7.6 Mc	8.5	$47.9 \pm 11.0$			
7.6 Md	13	$114.1 \pm 12.1$			
$f_{238}/^{238}U_0 (yr^{-1})$	$F^{234}U/F^{238}U$	$k^{238}U (yr^{-1})$	$k^{234}U/k^{238}U$		
$2.02 \pm 0.80 \times 10^{-5}$	$1.03 \pm 0.05$	$1.39 \pm 0.63 \times 10^{-5}$	$1.05\pm0.08$		
7.6 H				$0.17 \pm 0.10$	0.87
7.6 Ha	1	$18.4 \pm 4.2$			
7.6 Hb	6	$33.3 \pm 5.8$			
7.6 Hc	10	$54.2 \pm 5.4$			
$f_{238}/^{238}U_0 (yr^{-1})$	$F^{234}U/F^{238}U$	$k^{238}U (yr^{-1})$	$k^{234}U/k^{238}U$		
$2.45 \pm 1.27 \times 10^{-5}$	$1.04 \pm 0.06$	$1.62 \pm 1.04 \times 10^{-5}$	$\boldsymbol{1.08 \pm 0.18}$		
7.5 L1				$0.08\pm0.03$	0.70
7.5 La	3	$84.6 \pm 27.2$			
7.5 Lb	8	$77.8 \pm 27.0$			
7.5 Lc	13	$113.6 \pm 29.7$			
7.5 Ld	18	$160.8 \pm 30.3$			
7.5 Le	23	$337.1 \pm 167.6$			
$f_{238}/^{238}U_0 (yr^{-1})$	$F^{234}U/F^{238}U$	$k^{238}U (yr^{-1})$	$k^{234}U/k^{238}U$		
$1.67 \pm 0.66 \times 10^{-5}$	$1.33 \pm 0.21$	$1.38 \pm 0.57 \times 10^{-5}$	$1.38 \pm 0.22$		
7.5 L2				$0.06\pm0.03$	0.78
7.5 Lg	2	$69.4 \pm 44.4$			
7.5 Lh	7	$182.8 \pm 50.4$			
7.5 Lj	17	$310.7 \pm 69.3$			
7.5 Lk	22	$270.7 \pm 75.1$			
$f_{238}/^{238}U_0 (yr^{-1})$	$F^{234}U/F^{238}U$	$k^{238}U (yr^{-1})$	$k^{234}U/k^{238}U$		
$1.55 \pm 1.80 \times 10^{-5}$	$1.16\pm0.16$	$1.33 \pm 1.56 \times 10^{-5}$	$1.21\pm0.19$		

The model is solved as described in Appendices C and D.  $^{238}$ U<sub>0</sub> is initial number of 238U atoms/g in the starting material of the system. All the other parameters are described as in the text.

surrounding soil. In fact, the low and medium curvature transects on clast AN-14-7.6 (~13 mm and 15 mm thick) yield similar total weathering ages of ∼120 kyr while the high curvature transect (~10 mm thick) has a much younger total weathering age of only ~54 kyr (Table 3). Such a discrepancy is attributed to the loss of rind material from the high curvature profile (the "corner" site). Indeed, the study clast shows evidence of rind loss on the corner site (Fig. 3). Similar loss of rind material can also be inferred from clast AN-14-7.5: the two thick low-curvature transects (~23 mm thick) have similar total weathering ages of ~300 kyr (Table 3), while one high curvature transect (Fig. 3) shows a much thinner rind at the corner site. Nevertheless, the age-distance relationship determined based on the remaining rind (Fig. 12) still allows for a direct comparison of rind formation rates, or weathering advance rates

for the five rind transects as the visually defined core-rind boundary marks the starting point of weathering.

Although we assume that diffusion is the main transport mechanism across the rind, we assume the rind grew at a rate that was constant in time as shown previously (e.g., Sak et al., 2004; Pelt et al., 2008; Reeves and Rothman, 2014; Lebedeva et al., 2015). We therefore use a linear regression to calculate the rind formation rate, or the weathering advance rates for the five transects (Fig. 12). For clast AN-14-7.6, the rind on the high curvature transect  $(K = \sim 0.43 \text{ mm}^{-1})$  shows a linear distance vs. age relationship  $(R^2 = 0.87)$  and a weathering rate of  $0.17 \pm 0.10 \text{ mm/kyr}$ . Most of the rind on the low- and medium-curvature transects of AN-14-7.6 also show linear distance vs. age relationships: the medium-curvature transect  $(K = \sim 0.16 \text{ mm}^{-1})$  shows a weathering rate of

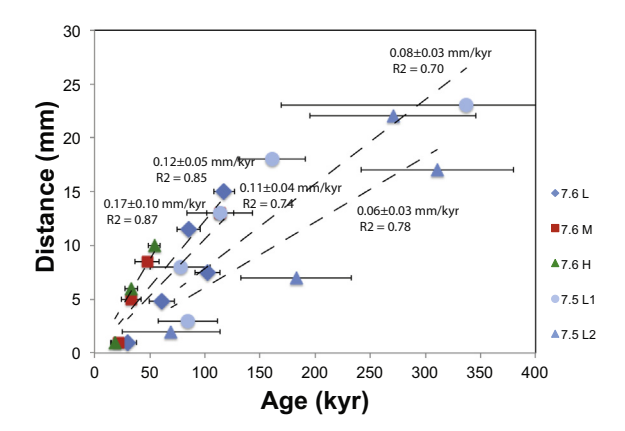


Fig. 12. Rind formation age (i.e., weathering exposure ages) plotted as a function of position relative to the core—rind boundary for the low, medium, and high curvature transect on clast AN-14-7.6 and the two low curvature transects on AN-14-7.5. Dashed lines represent a linear regression to each transect. Regressions were forced through the origin as we define position 0 as the start point (t=0) for chemical weathering.

 $0.12\pm0.05~(R^2=0.85)$  and the low-curvature transect  $(K=\sim0.01~{\rm mm^{-1}})$  shows a weathering rate of  $0.11\pm0.04~(R^2=0.74)$ . Both rates are slower than the rate of the high curvature transect for AN-14-7.6. The slower weathering advance rates on the low curvature transects can also be confirmed by the results from clast AN-14-7.5: both transects are located on low curvature sites and have weathering advancing rates of  $0.08\pm0.03~(R^2=0.70)$  and  $0.06\pm0.03~(R^2=0.78)$ , respectively. Hence, at the clast scale, the weathering rates decrease with decreasing curvature of the core-rind boundary for both clasts.

The dependency of weathering rates on curvature at the clast scale is consistent with the observations from the elemental depletion profiles (Figs. 5-7). In other words, the high curvature site is characterized by a fast weathering rate that may result in a steep depletion curve (or a narrow weathering front). As concluded in the previous studies (Sak et al., 2010; Navarre-Sitchler et al., 2009, 2011; Ma et al., 2012), as the low porosity of the basaltic andesite core and innermost rind materials precludes fast rates of advective transport to the reaction front, the transport mechanism was inferred to be diffusion. For such a diffusion system, a higher curvature interface allows reactant to reach the weathering interface (or product to diffuse away) at a faster rate than a lower curvature/planar interface and hence results a higher weathering advance rate. Indeed, recent modeling results predict a positive correlation between the weathering advance rate  $(\omega_n)$  and the curvature of a weathering interface for a weathering clast:  $\omega_n = \omega_0 + |K|D\phi(C^e - C^R)/Q^0$  (Eq. (30) in Lebedeva et al., 2015). Here  $\omega_0$  is the advance rate of a planar front; D is the diffusivity of solutes and  $\phi$  is porosity of the weathering material as defined above;  $C^e$  and  $C^R$  are the equilibrium solute concentration and the solute concentration at the interface during dissolution, respectively;  $Q^0$  is the concentration of reactive minerals in the parent material. The strong dependency of weathering advance rates on curvature as observed from this U-series disequilibria study is well supported by the modeling results by Lebedeva et al. (2015). Indeed, these new U-series data provide direct evidence that the curvature of the interface controls the rate of weathering advance of the rind at the clast scale. This study confirms previous findings by our group (Ma et al., 2012), that weathering rates at the clast scale can be directly determined by using U-series disequilibria in weathering rinds. This is also the first field study in which multiple weathering clasts from the same site were analyzed with the U-series disequilibria and yielded consistent weathering ages and rates, highlighting a new field tool to measure long-term chemical weathering rates in solid-state weathering products.

# 5.4. Weathering advance rates across a gradient of precipitation on Basse-Terre Island

The rind formation rates in the relatively low precipitation Deshaies watershed range from  $\sim\!0.06$  to 0.17 mm/kyr for the low-, medium-, and high-curvature sites on the corerind boundary for both studied clasts. The three low curvature transects (i.e. with a planar core-rind boundary) are characterized by consistently low weathering advance rates for the rind (0.06, 0.08, and 0.11 mm/kyr). The average weathering advance rate (0.08  $\pm$  0.03 mm/kyr) of the low curvature sites in the Deshaies watershed is about 60% slower than the rind formation rate in the Bras David watershed (0.18  $\pm$  0.07 mm/kyr, previously determined in the wetter watershed on Basse-Terre Island by Ma et al., 2012), although both estimates have relatively large associated uncertainties (Fig. 13). The weathering advance rates

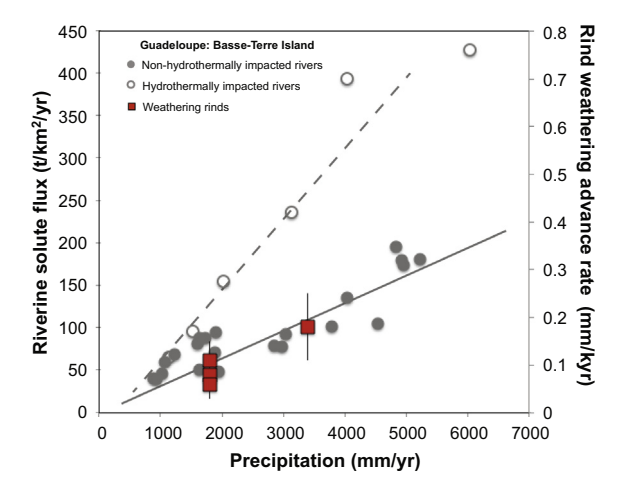


Fig. 13. Riverine solute fluxes and rind weathering advance rates as a function of watershed precipitation on Basse-Terre Island. Riverine flux values are shown for major rivers on Basse-Terre Island (Gaillardet et al., 2011). Rivers that are not impacted by hydrothermal activities (close gray circles) define a linear relationship (solid gray line). Hydrothermal impacted rivers (open gray squares) show a different linear relationship (dashed gray line). Rind weathering advance rates for low curvature rind-core boundary (close red squares) for Deshaies (this study) and Brad David (Ma et al., 2012) watersheds show a linear relationship with a similar slope to the riverine study (Gaillardet et al., 2011).

on the high curvature site of the Deshaies clast (0.17 mm/kyr) is also similarly 30% slower than the high curvature site of the Bras David clast (0.24 mm/kyr), although the curvature values of these two sites are not exactly the same. As both watersheds have a similar MAT (23 °C) but the Deshaies watershed has MAP (1800 mm) that is nearly 50% lower than the Bras David Watershed (3400 mm), such a comparison is consistent with a measurable effect of precipitation on chemical weathering over these long time scales (Fig. 13).

It is well known that the influx of precipitation is an important control on the chemistry of streams and rivers (e.g., Godsey et al., 2009; Maher, 2010; Eiriksdottir et al., 2013; Maher and Chamberlain, 2014). Indeed, as Lebedeva et al. (2015) documented in their Eq. (30), the rate of weathering advance for a rind on a clast is determined not only by curvature (K) and mineralogical content  $(Q^0)$ , and solute transport characteristics (D), but also by solute concentrations. Specifically the rate of advance is predicted to be a direct function of a term  $(C^e - C^R)$ , which expresses the difference in the equilibrium concentration of the reactive component (a constant for constant temperature systems) and the concentration of this component in the pore fluid at the outermost boundary of the weathering clast. Watersheds weathering at the same temperature but with higher precipitation are expected to have more dilute soil water at any given depth and therefore higher values of  $(C^e - C^R)$ . If  $(C^e - C^R)$  varies linearly with MAP, then the Lebedeva et al. model is consistent with a linear increase in weathering advance rates during rind formation according to their Eq. (30).

In fact, river chemistry data of Basse-Terre Island (Fig. 13) has shown that the Deshaies watershed is characterized with a catchment-wide chemical weathering rate (46 t/km²/yr) about 50% lower than the calculated rate (92 t/km²/yr) for the Bras David watershed (Gaillardet et al., 2011). The newly determined weathering advance rates from weathering rinds confirm the previously observed relationship between precipitation and river weathering fluxes at Basse-Terre Island. Notably, the weathering advance rates were determined in rinds without using the river runoff values. Their correlation between weathering and MAP in watersheds does not involve the same complications as using the riverine weathering fluxes. This weathering rind based approach thus has the potential to serve as a strong complement to riverine studies.

Furthermore, the rind weathering advance rates were determined for a time scale of hundreds of thousands years; i.e. the rate was averaged over the total weathering duration of the rind in the last 100 kyr (Fig. 12), much longer than the contemporary chemical weathering fluxes measured in river chemistry. Multiple glacial-interglacial cycles have occurred over that interval and absolute precipitation values could have varied on the island, e.g. alternating dry and wet climate during glacial and interglacial cycles. However, the observation of MAP-dependent rind weathering rates are consistent with a precipitation gradient, e.g. the dry to wet gradient from the north to south on the island, that prevailed over the last  $\sim 100$  kyr. In other words, even if the absolute magnitude of precipitation changed over the

last 100 kyr, a gradient has been maintained. One possible explanation is that the spatial precipitation pattern is largely controlled by the topographic gradient of the island that is controlled by the balance between relief construction (volcanic activity) and destruction (chemical and physical erosion) and has likely to remain constant through the last 100 kyr. Combined with the river chemistry study, the rind study demonstrates the importance of the water cycle in controlling chemical weathering and CO<sub>2</sub> consumption over long timescales (Fig. 13; e.g. Gaillardet et al., 2011).

# 5.5. Comparison of chemical weathering rates normalized to surface areas with different spatial scales

The study of weathering rinds also expands our field toolbox to compare chemical weathering rates across different spatial scales (e.g. Fig. 13). In the Deshaies watershed, the rind weathering rates (0.06–0.17 mm/kyr, or mm<sup>3</sup> mm<sup>-2</sup> clast area kyr<sup>-1</sup>), when renormalized by clast surface area, correspond to chemical weathering rates of ~0.02-0.04 ton/km<sup>2</sup><sub>clast area</sub>/yr. This calculation entails the multiplication of the rind weathering rate by parent rock density, 2600 kg/m<sup>3</sup>. In turn, this rate is then multiplied by the mass fraction of total cations, 0.1, i.e. mass of Na + K + Mg+ Ca lost from the mass of rock (Ma et al., 2012). The rind weathering rates at the clast scale are approximately 1200-2300 times slower than the weathering rate determined at the watershed scale (46 t/km<sup>2</sup><sub>watershed</sub>/yr; normalized by the geographic area of the watershed). This comparison is based on the implicit assumption that the weathering rates determined from two clasts are representative of the studied catchment. Similarly, the rind weathering rates in the Bras David watershed are 1100-2000 times slower than the weathering rate determined at the catchment scale (Ma et al., 2012).

Such a discrepancy is largely due to the fact that the surface areas are measured by the use of different "rulers" at different spatial scales (Navarre-Sitchler and Brantley, 2007). Overall, laboratory- and field-based chemical weathering rates generally do not agree and the discrepancy (several orders of magnitude difference) has been attributed to differences such as duration of weathering (White and Brantley, 2003; Maher et al., 2004), hydrologic regime and flow path factors (Velbel, 1993; Pacheco and Alencoao, 2006; Zhu, 2009), factors related to clay precipitation (Maher, 2010), and methods used to measure surface area or the presence of surface coatings (Nugent et al., 1998; Maher et al., 2006; Navarre-Sitchler and Brantley, 2007), the influence of biota or organic acids (Wasklewicz, 1994; Drever and Stillings, 1997), and ongoing removal of weathered materials by physical erosion (i.e., Bluth and Kump, 1994; Millot et al., 2002; Dupre et al., 2003; Anderson, 2005; West et al., 2005). However, in a different approach to this problem, Navarre-Sitchler and Brantley (2007) assumed that the rate of weathering of basalt was constant when compared across scales from the laboratory to clasts to soil profiles to watersheds when normalized by the basalt surface area that experienced weathering ( $A_{weathering}$ ). At each scale, the weathering rate was reported as a rate normalized by  $A_{weathering}$  assessed

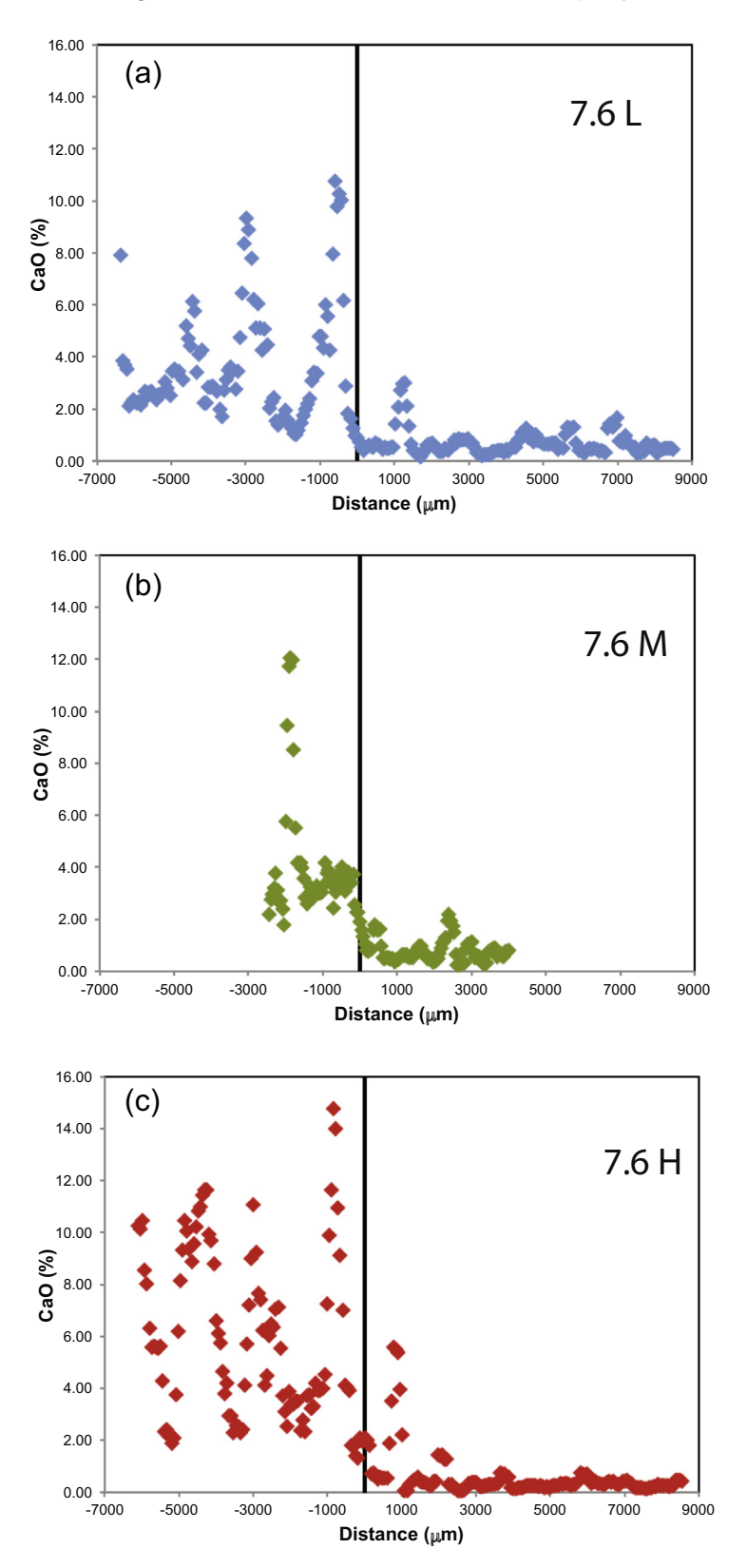


Fig. A1. EMP point measurements of CaO (%) concentrations for (a) low, (b) medium, and (c) high curvature transect (L, M, and H lines in Fig. 4) on clast AN-14-7.6. Vertical line at distance = 0 mm is visually defined core-rind boundary.

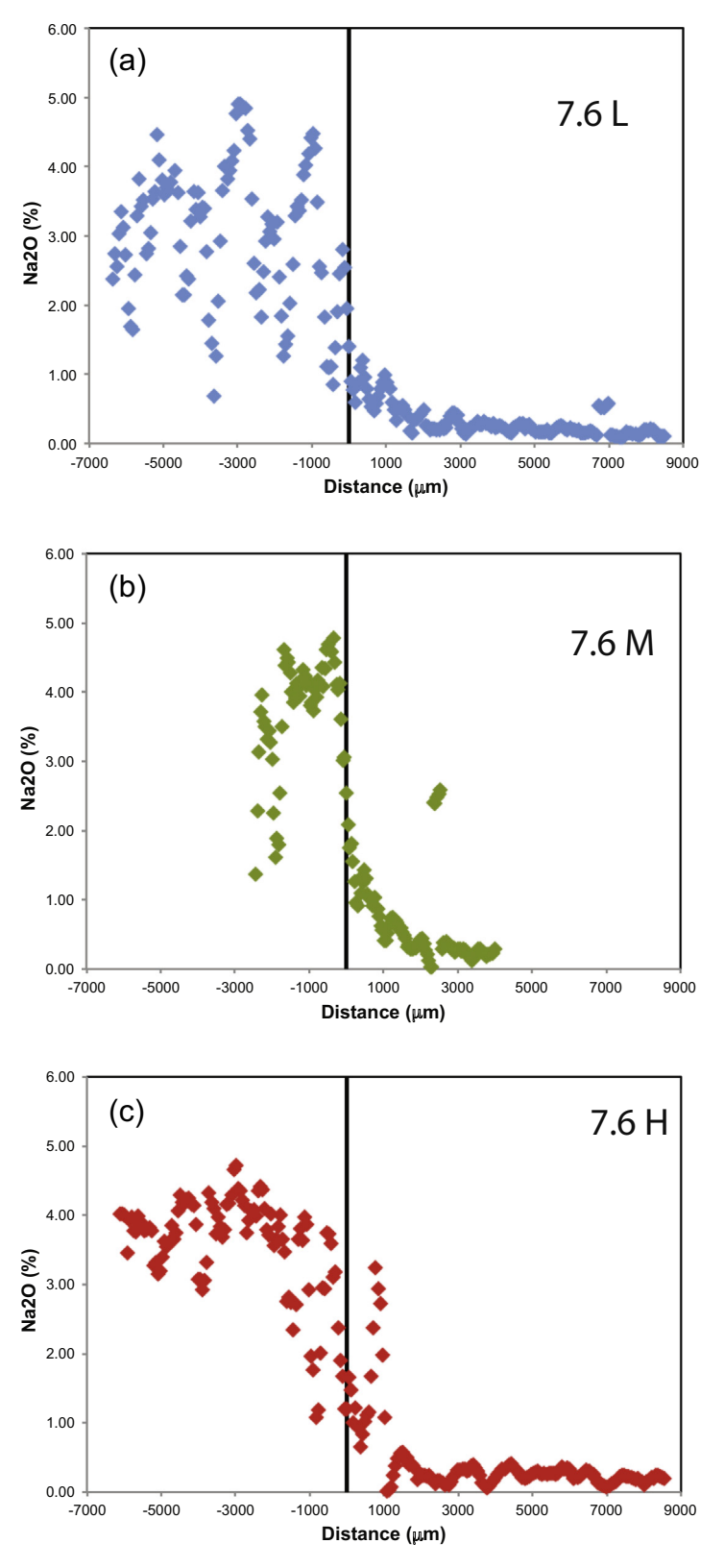


Fig. A2. EMP point measurements of  $Na_2O$  (%) concentrations for (a) low, (b) medium, and (c) high curvature transect (L, M, and H lines in Fig. 4) on clast AN-14-7.6. Vertical line at distance = 0 mm is visually defined core—rind boundary.

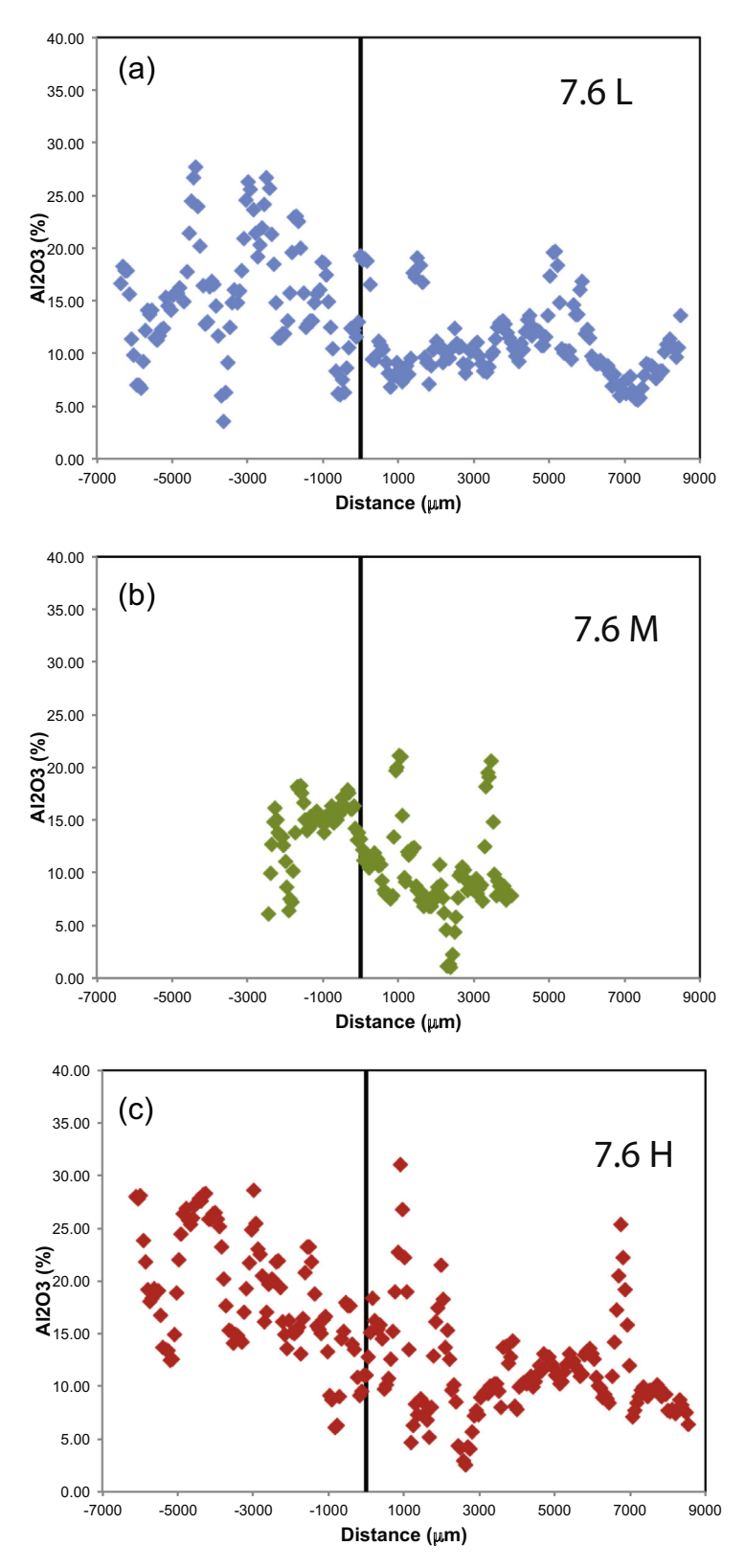


Fig. A3. EMP point measurements of Al2O3 (%) concentrations for (a) low, (b) medium, and (c) high curvature transect (L, M, and H lines in Fig. 4) on clast AN-14-7.6. Vertical line at distance = 0 mm is visually defined core—rind boundary.

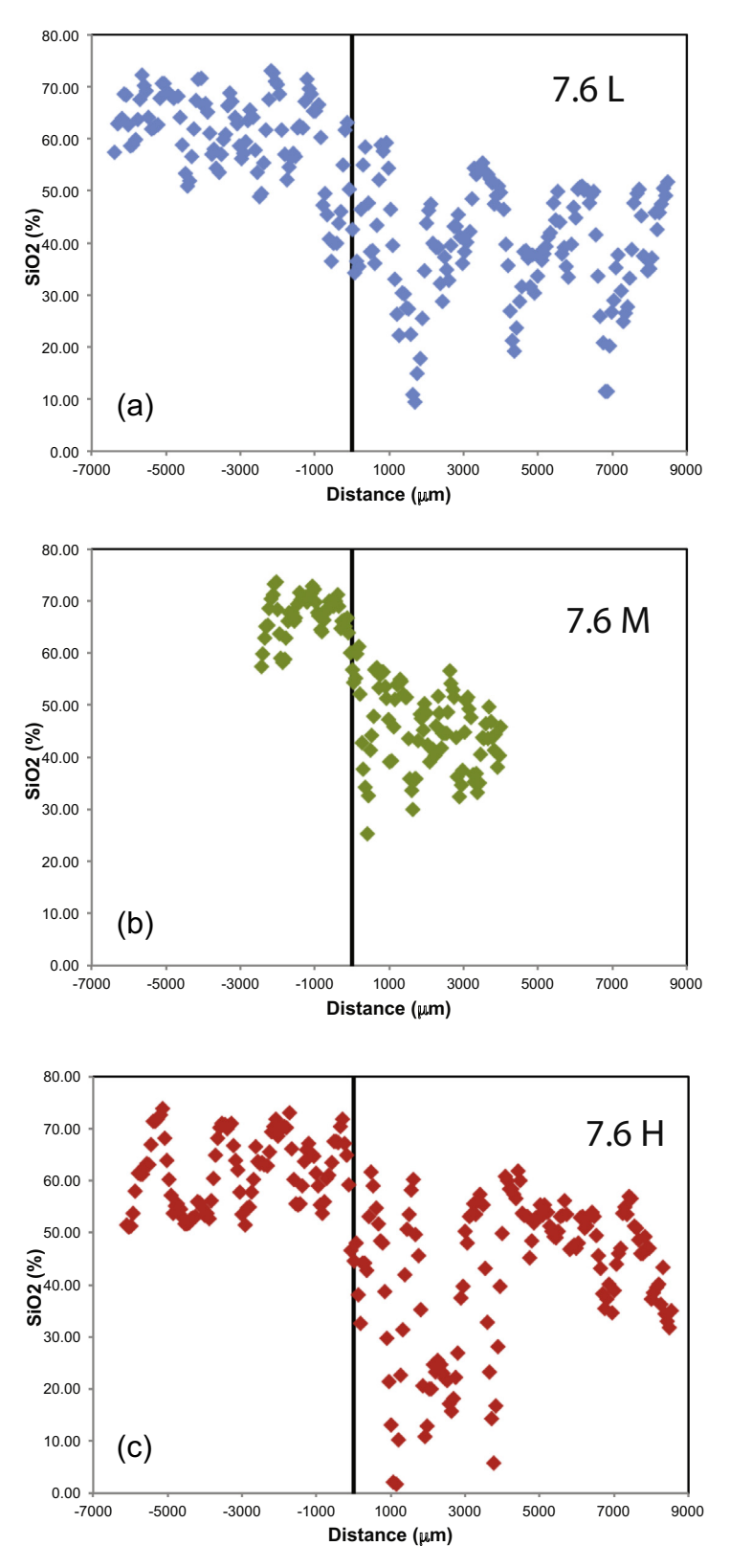


Fig. A4. EMP point measurements of SiO2 (%) concentrations for (a) low, (b) medium, and (c) high curvature transect (L, M, and H lines in Fig. 4) on clast AN-14-7.6. Vertical line at distance = 0 mm is visually defined core—rind boundary.

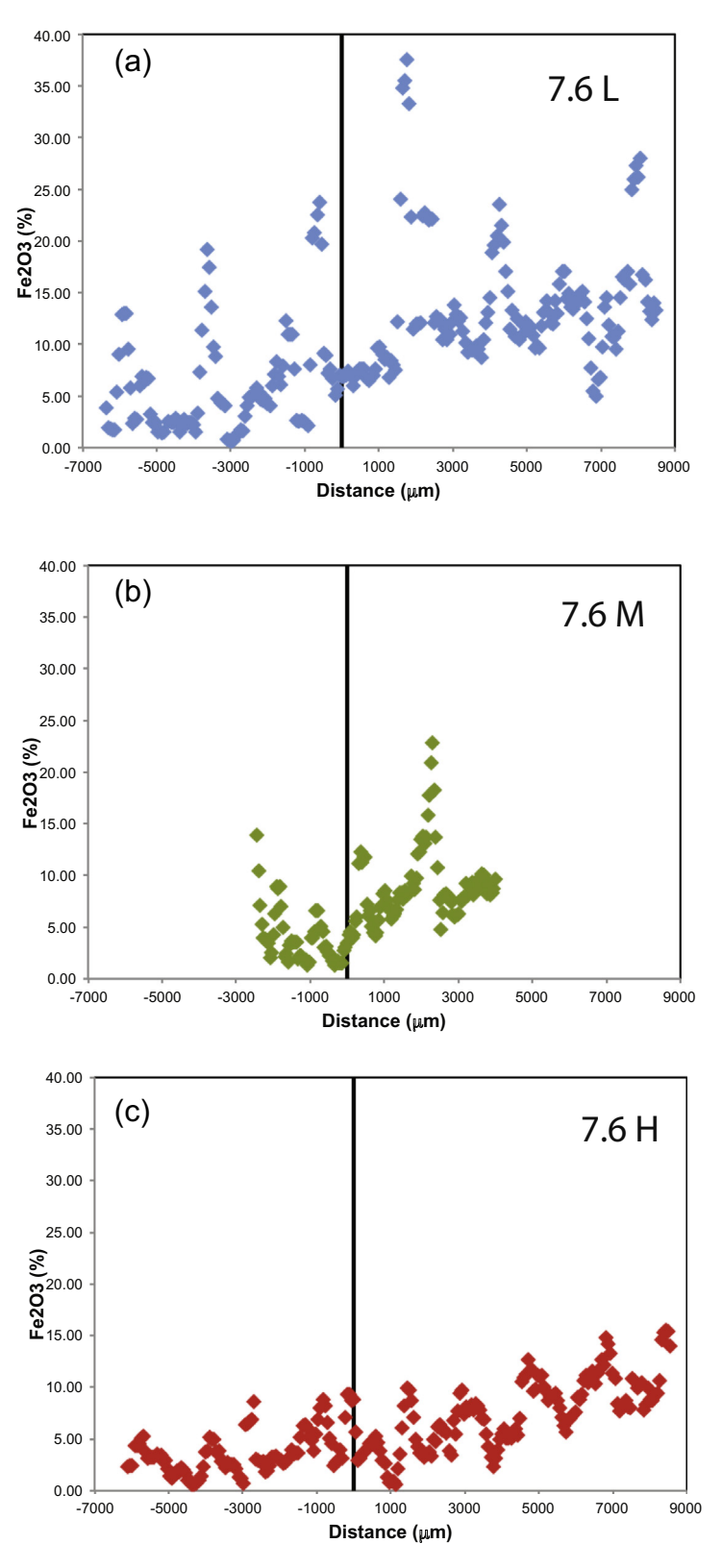


Fig. A5. EMP point measurements of Fe2O3 (%) concentrations for (a) low, (b) medium, and (c) high curvature transect (L, M, and H lines in Fig. 4) on clast AN-14-7.6. Vertical line at distance = 0 mm is visually defined core-rind boundary.

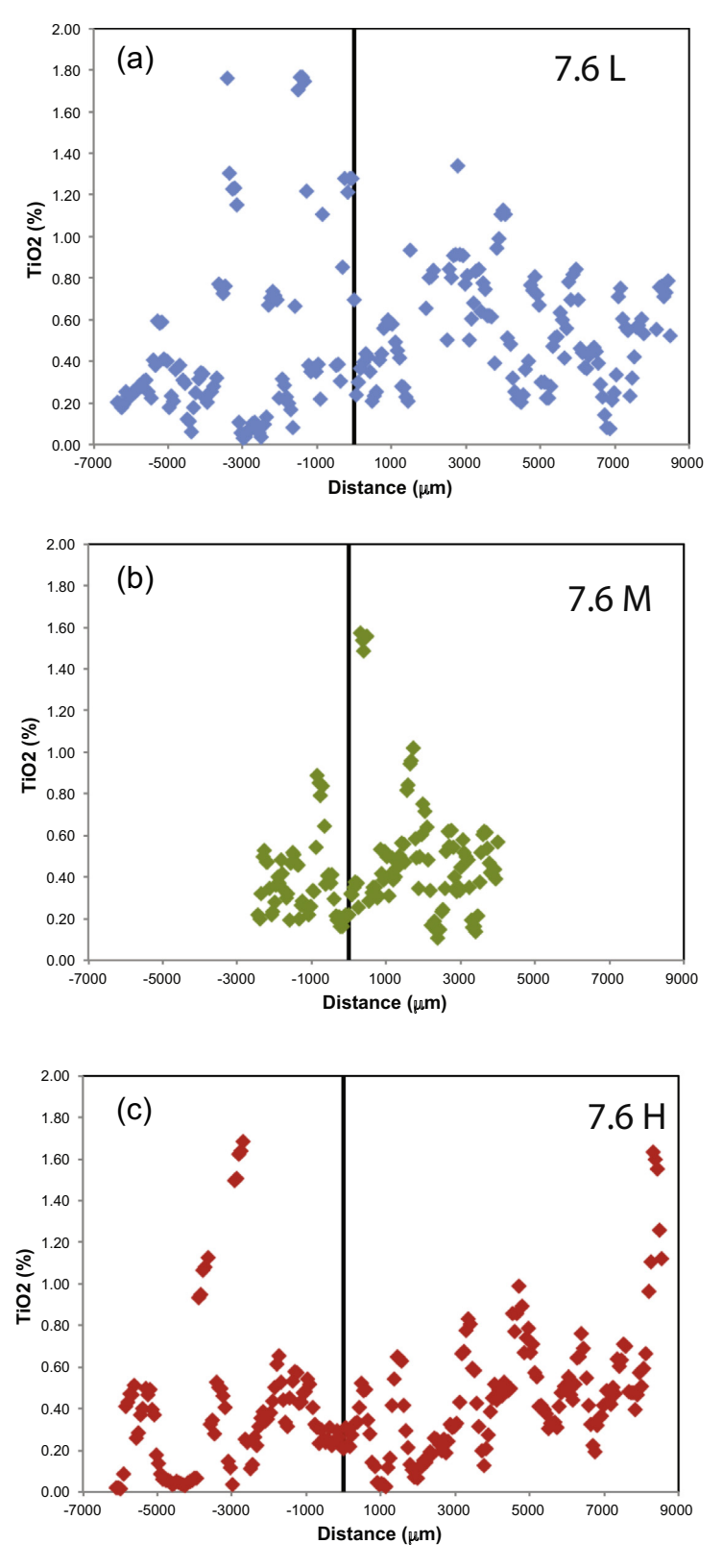


Fig. A6. EMP point measurements of TiO2 (%) concentrations for (a) low, (b) medium, and (c) high curvature transect (L, M, and H lines in Fig. 4) on clast AN-14-7.6. Vertical line at distance = 0 mm is visually defined core—rind boundary.

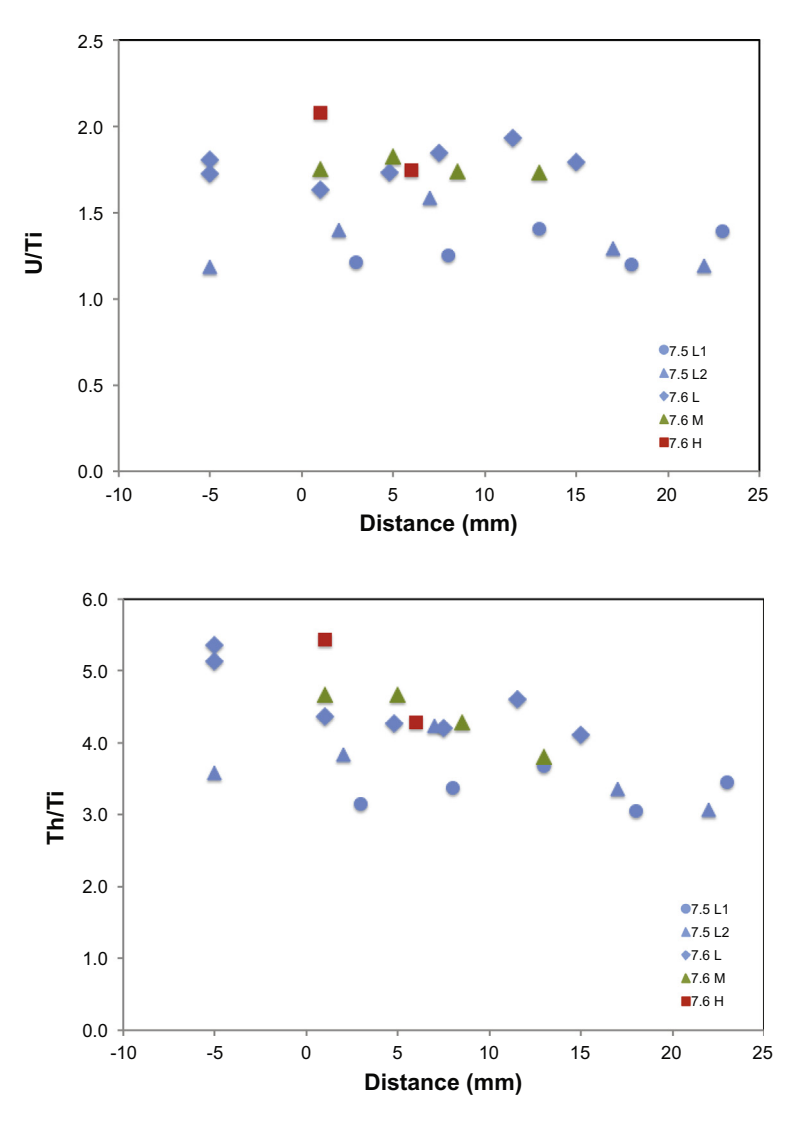


Fig. B1. Elemental ratios of U/Ti and Th/Ti plotted as a function of position relative to the core—rind boundary (indicated as position 0) for the low (L), medium (M), and high H) curvature transect of clast AN-14-7.6 and the low curvature transects of clast AN-14-7.5. For clast 7.6, the U/Ti ratios of the Low curvature (L) transect show an increase trend from the core to the rind, suggesting addition of U into the rind relative to Ti. The U/Ti ratios of the Medium curvature (M) transect only show a slight increase trend near the core-rind boundary and then a decrease trend in the outer rind. The U/Ti ratios of the High curvature (H) transect first show an increase and then decrease trend. Both transects of the clast 7.5 show very similar increasing trends of U/Ti ratios: an increasing trend (L1), and an increase first then decrease trend (L2). Hence, the variations of U/Ti ratios with distance suggest that U is more mobile than Ti and in general, there is an increase of U/Ti ratios, suggesting that U is added into the rind, with respect to Ti. The reason that we don't observe a nice linear increase in the U/Ti ratios as in the U/Th ratios is due to the analytical issues that U—Th and Ti were not measured in the same sample or by the same analytical method. Similarly, we assume that Th is as immobile as Ti and thus expect to see invariable Th/Ti ratios from the core to the rind, implying that Th may be more mobile than Ti. However, in Clast 7.6, we observe decreasing Th/Ti ratios from the core to the rind, implying that Th may be more mobile than Ti. However, in Clast 7.5, we don't observe such a decreasing trend, we see quite invariable Th/Ti ratios as expected. The fact that Th/Ti ratios behave quite different in these two clasts (i.e. no systematic mobility trends in both clasts) may suggest that the rather large variability in clast 7.6 is an artifact, due to the use of Th and Ti concentrations from two different sets of samples. The observation from clast 7.5 confirms the same immobile behavior of Th as Ti

at that spatial scale: for example, the geographic area of a watershed ( $A_{weathering} = A_{watershed}$ ) or the surface area estimated from the geometry of a clast ( $A_{weathering} = A_{clast}$ ). These surface area measurements are not comparable in magnitude but are fractal in that they vary with the scale of measurement. For any given comparison, for example

between a watershed and a clast, Navarre-Sitchler and Brantley (2007) defined the ratio of  $A_{watershed}/A_{clast}$  as the roughness ( $\lambda$ ) value. This definition was posed by analogy to the common definition of surface roughness for a mineral grain as the ratio of the BET surface area of the grain divided by its geometric surface area. In the Deshaies

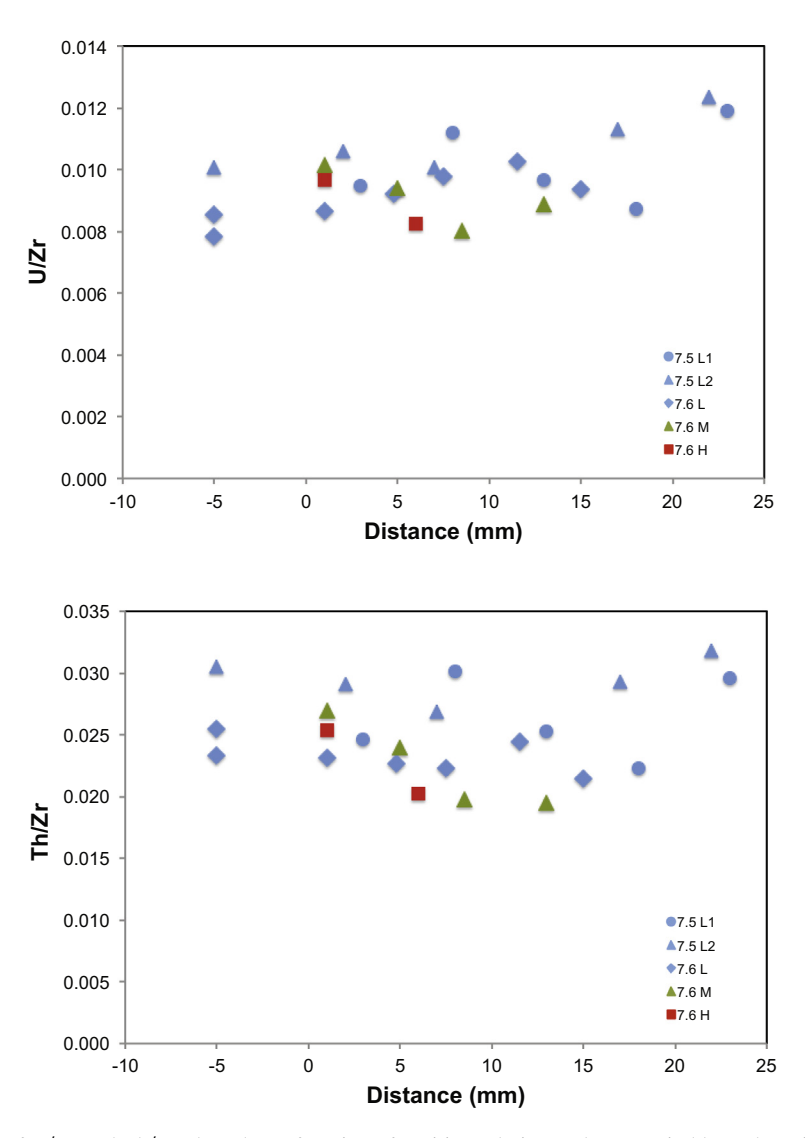


Fig. B2. Elemental ratios of U/Zr and Th/Zr plotted as a function of position relative to the core—rind boundary (indicated as position 0) for the low (L), medium (M), and high (H) curvature transect of clast AN-14-7.6 and the low curvature transects of clast AN-14-7.5. U is in generally added to rind while Th is immobile as expected. The large scatters of the U/Zr and Th/Zr ratios are due to the same analytical issues that we explained before (U-Th and Zr were not measured in the same sample or by the same analytical method).

watershed, the discrepancy between watershed rates and clast rates can be reconciled if the surface roughness ( $\lambda$ ) equals approximately 1200–2300, which is nearly identical to the roughness value (1100–2000) estimated for the Bras David watershed (Ma et al., 2012). It is noted that the roughness value estimated here may also include factors related to flow path and residence time, in addition to the surface area factor. For the purpose of discussion here, the roughness from the catchment to the clast scale is simply assumed to be the ratio of the entire dissolving rock—water interfacial area in a catchment compared to the similar interfacial area of one clast. This new calculation implies that the roughness values remain constant for watersheds on Basse-Terre Island and may not change with

precipitation. U-series isotope systematics in weathering rinds provides a new tool to compare how weathering interface advances at difference spatial scales and to understand how surface roughness is developed at the watershed scale.

### 6. CONCLUSIONS

To further investigate whether U-series disequilibria in weathering rinds can be used to determine changes of long-term weathering rates as a function of precipitation, we systematically studied two weathering clasts collected from the Deshaies watershed (MAP = 1800 mm and MAT =  $23 \,^{\circ}\text{C}$ ) on the Basse-Terre Island. Five rind tran-

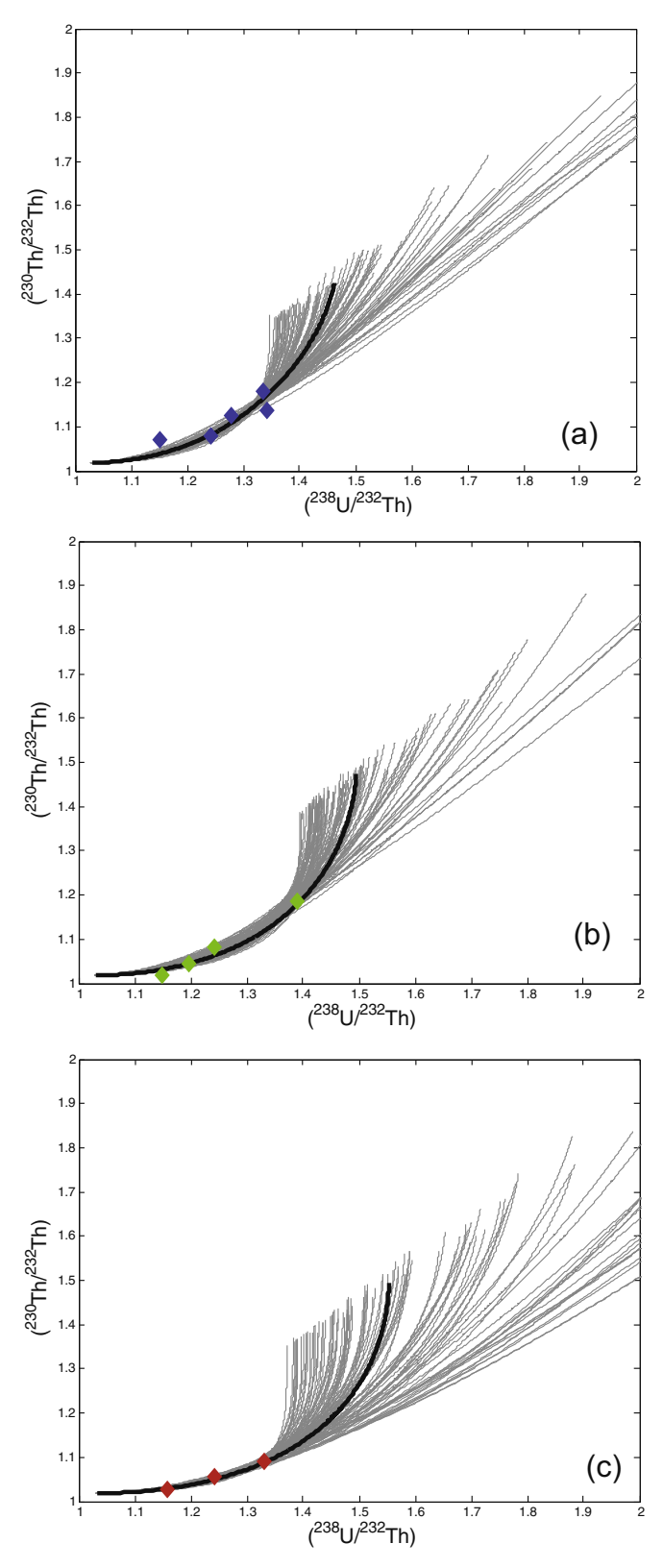


Fig. C1.  $(^{230}\text{Th}/^{232}\text{Th})_a$  vs.  $(^{238}\text{U}/^{232}\text{Th})_a$  isochron diagram for (a) low, (b) medium, and (c) high curvature transects of clast AN-14-7.6. The U–Th radioactive disequilibrium of the weathering rind samples from all three transects is explained by (1) continuous input of U plus leaching of U starting at the core–rind boundary (without addition or loss of Th), and (2) subsequent production of  $^{230}\text{Th}$  from U-series decay series in the rind. Rind formation ages were determined by an open-system U addition model (see text and Appendix C for details). When the model is solved (Table 3), the activity ratios of  $(^{238}\text{U}/^{232}\text{Th})$  and  $(^{230}\text{Th}/^{232}\text{Th})$  are calculated as a function of rind formation ages and are shown as the gray lines. The thin gray lines indicate model results for 100 sets of solutions. The thick black lines indicate the model results with the median and stand deviations of the 100 sets of solutions (Table 3).

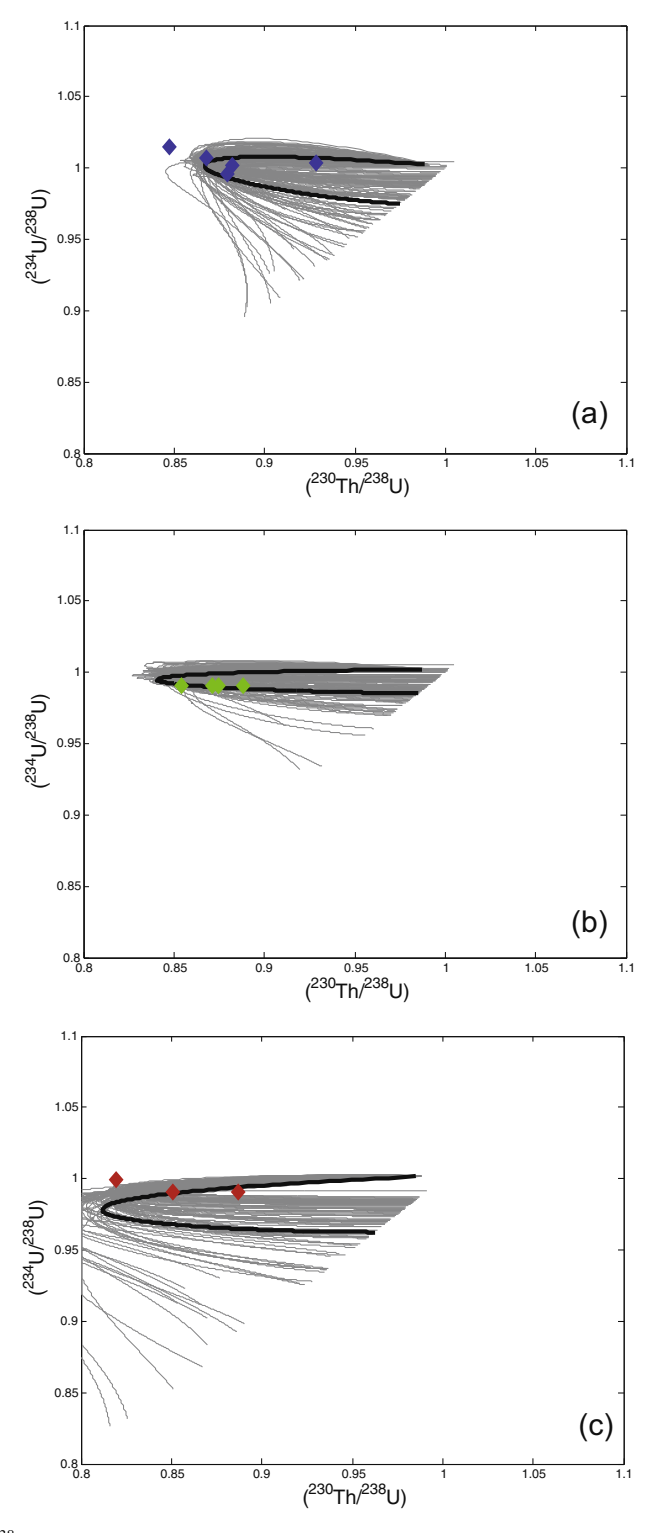


Fig. C2.  $(^{230}\text{Th}/^{238}\text{U})_a$  vs.  $(^{234}\text{U}/^{238}\text{U})_a$  isochron diagram for (a) low, (b) medium, and (c) high curvature transects of clast AN-14-7.6. The U—Th radioactive disequilibrium of the weathering rind samples from all three transects is explained by (1) continuous input of U plus leaching of U starting at the core—rind boundary (without addition or loss of Th), and (2) subsequent production of  $^{230}\text{Th}$  from U-series decay series in the rind. Rind formation ages were determined by an open-system U addition model (see text and Appendix C for details). When the model is solved (Table 3), the activity ratios of  $(^{230}\text{Th}/^{238}\text{U})$  and  $(^{234}\text{U}/^{238}\text{U})$  are calculated as a function of rind formation ages and are shown as the gray lines. The thin gray lines indicate model results for 100 sets of solutions. The thick black lines indicate the model results with the median and stand deviations of the 100 sets of solutions (Table 3). The data points show more scatters to the model results than the previous  $(^{230}\text{Th}/^{232}\text{Th})_a$  vs.  $(^{238}\text{U}/^{232}\text{Th})_a$  diagram (Fig. C1) and is due to the fact that only  $(^{234}\text{U}/^{238}\text{U})$  ratios were used as the constraining parameter while both  $(^{230}\text{Th}/^{232}\text{Th})_a$  vs.  $(^{238}\text{U}/^{232}\text{Th})_a$  ratios were used as the constraining parameters in the previous diagram (Fig. C1).

sects with distinct curvatures on the rind-core boundary for the clasts were characterized by petrographic, bulk chemical, electron microprobe, and U-series isotope analyses. This is the first time that multiple weathering clasts from the same watershed were systematically analyzed to study chemical weathering and consistent results were obtained.

Combined EMP observations and major element profiles reveal that the extent of elemental loss during rind formation decreases in the order  $Ca \approx Na \approx > K \approx Mg > Si \approx Al > Zr \approx Ti \approx Fe$ . Such an order suggests the sequence of weathering reactions as: glass and groundmass matrix and primary minerals (plagioclase, pyroxene) weather to produce Fe oxyhydroxides, gibbisite and minor kaolinite, with the reactivity of phases decreasing in the order, plagioclase  $\approx$  pyroxene  $\approx$  glass matrix  $\gg$  ilmenite.

Significant U-series disequilibria are documented in both weathering rinds, as a result of the unique mobility behavior of U-series isotopes during weathering including: (1) fractionation of <sup>234</sup>U and <sup>238</sup>U isotopes during chemical leaching, (2) addition of <sup>234</sup>U and <sup>238</sup>U isotopes into weathering rinds by circulating soil pore water, and (3) radioactive production of <sup>230</sup>Th and the immobile nature of <sup>230</sup>Th and <sup>232</sup>Th isotopes during rind formation. The creation of U-series disequilbria is closely linked to the rind formation processes that started at the core-rind boundary, including creation of porosity, infiltration of soil pore water, and formation of Fe-Al oxides. The U-series disequilibria allow for determination of rind formation ages and weathering advance rates for the five rind transects. The weathering rates show a systematic decrease with decreasing curvature:  $\sim 0.17 \pm 0.10$  mm/kyr for the high curvature profile,  $\sim 0.12 \pm 0.05$  mm/kyr for the medium curvature profile, and  $\sim 0.11 \pm 0.04$ ,  $\sim 0.08 \pm 0.03$ ,  $\sim 0.06$  $\pm 0.03$  mm/kyr for the three low curvature profiles. Both the U-series disequilibria results and the elemental profiles are consistent with weathering rates and weathering front thicknesses varying with the curvature of the rind-core boundary at the clast scale. The observed positive correlation between the curvature and the weathering rates is well supported by the prediction in a previous numerical modeling study (Lebedeva et al., 2015). At the watershed scale, new weathering rates of low curvature transects derived for the relative dry Deshaies watershed  $(\sim 0.08 \text{ mm/kyr}; \text{MAP} = 1800 \text{ mm} \text{ and MAT} = 23 \,^{\circ}\text{C})$  are  $\sim$ 60% slower than the weathering rind formation rates in wet Bras David watershed  $(\sim 0.18 \text{ mm/kyr};$ MAP = 3400 mm and  $MAT = 23 \degree C$ ) of Basse-Terre Island. Such a observation is consistent with the differences in riverine chemical weathering fluxes between these two watersheds (Gaillardet et al., 2011). The new weathering rates from the weathering rinds confirm that U-series disequilibria document the changes of weathering rates as a function of precipitation, highlighting the important role of precipitation on controlling weathering rates on this island over a long time scale on the order of  $\sim 100 \text{ kyr}$ . Weathering rinds thus provide a suitable system for investigating long-term chemical weathering across environmental gradients.

To fully utilize U-series disequilibria in weathering rinds as a new geochronometer, future rind studies could focus on understanding in detail the controlling factors on rind formation at soil profile scales (such as weathering clast sizes, relative clast locations in soil depths, difference in wetting/drying cycles, pH and redox conditions) with both field and numerical model studies.

#### ACKNOWLEDGEMENTS

This research was funded by the National Science Foundation grants EAR1251952 to L.M., EAR1251969 to P.B.S., and EAR1251875 to S.L.B., and. We thank Celine Dessert (IPGP) and L'Observatoire Volcanologique et Sismologique de Guadeloupe (IPGP) for providing logistical support. L.M. also acknowledged analytical assistant of Dr. Adam Ianno from Center of Earth and Environmental Isotope Research at UTEP. J.G. has benefited from a grant from Institut Universitaire de France. We thank Julien Bouchez and Johanna Noireaux (IPGP) for their help in the field and fruitful discussions. We also thank Sebastien Lambert

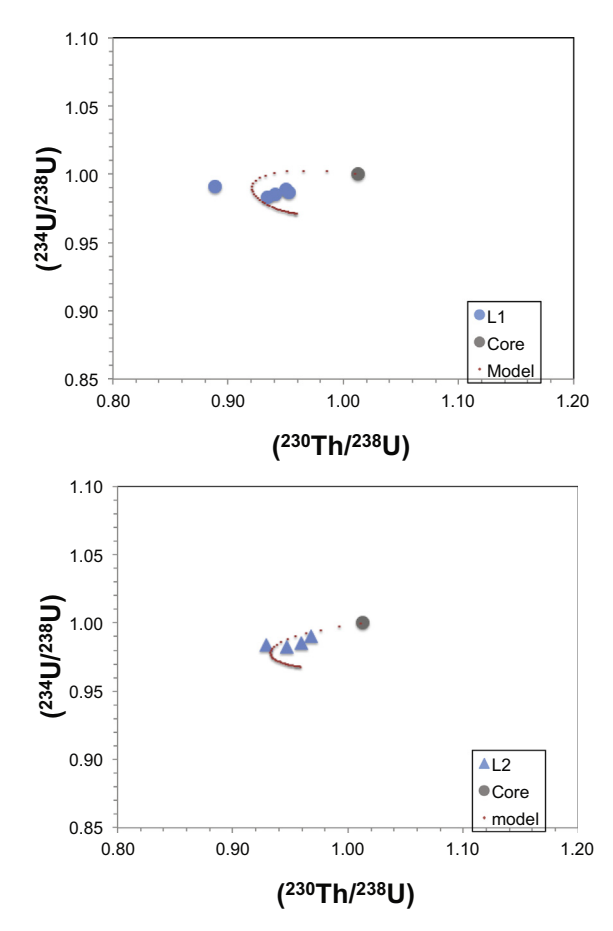


Fig. C3.  $(^{230}\text{Th}/^{238}\text{U})_a$  vs.  $(^{234}\text{U}/^{238}\text{U})_a$  isochron diagram for (a) L1 and (b) L2 low curvature transects of clast AN-14-7.5. Rind formation ages were determined by an open-system U addition model (see text and Appendix C for details). When the model is solved (Table 3), the activity ratios of  $(^{230}\text{Th}/^{238}\text{U})$  and  $(^{234}\text{U}/^{238}\text{U})$  are calculated as a function of rind formation ages and are shown as the dotted lines.

from the Societé Antillaise de Granulats in French Guadeloupe for the great logistical support.

Disclaimer — use of trade or product names is for descriptive purposes only and does not imply endorsement by the U.S. Government.

### APPENDIX A

See Figs. A1-A6.

### APPENDIX B

See Figs. B1 and B2.

#### APPENDIX C

#### Solving the continuous U addition and leaching model

We present here a solution to the continuous U-series addition and leaching model in Section 5.4. The model consists of the system of Eqs. (3)–(6) with unknown parameters for rind formation ages (t), addition rates of  $^{238}$ U and  $^{234}$ U ( $f_{238}$  and  $f_{234}$ ) and first-order leaching coefficients of  $^{234}$ U and  $^{238}$ U ( $k_{234}$  and  $k_{238}$ ). Terms  $\lambda_{238}$ ,  $\lambda_{234}$ ,  $\lambda_{230}$ , and  $\lambda_{232}$  are the decay constants for  $^{238}$ U,  $^{234}$ U,  $^{230}$ Th and  $^{232}$ Th (yr $^{-1}$ ), respectively. The ordinary differential Eqs. 3–6 were first solved analytically and rearranged to describe changes of ( $^{238}$ U/ $^{232}$ Th), ( $^{230}$ Th/ $^{232}$ Th), and ( $^{234}$ U/ $^{238}$ U) activity ratios for a weathering rind sample as a function of  $f_{238}$ ,  $f_{234}$ ,  $k_{234}$ ,  $k_{234}$ ,  $k_{238}$ , and t (Eqs. C1–C3):

$$\begin{pmatrix} \frac{238\,\mathrm{U}}{232\,\mathrm{Th}} \end{pmatrix}_{a} = \begin{pmatrix} \frac{238\,\mathrm{U}}{232\,\mathrm{Th}} \end{pmatrix}_{0} \left[ \left( 1 - \frac{f_{238}}{238\,\mathrm{U}_{0}a_{238}} \right) e^{(\lambda_{232} - a_{238})t} + \frac{f_{238}}{238\,\mathrm{U}_{0}a_{238}} e^{\lambda_{232}t} \right]$$

$$(C1)$$

$$\begin{pmatrix} \frac{230\,\mathrm{Th}}{232\,\mathrm{Th}} \end{pmatrix}_{a} = \begin{pmatrix} \frac{230\,\mathrm{Th}}{232\,\mathrm{Th}} \end{pmatrix}_{0} e^{(\lambda_{232} - \lambda_{230})t}$$

$$+ \begin{pmatrix} \frac{238\,\mathrm{U}}{232\,\mathrm{Th}} \end{pmatrix}_{0} \frac{\lambda_{230}\lambda_{234}}{\lambda_{230} - a_{234}} (e^{-a_{234}t} - e^{-\lambda_{230}t}) e^{\lambda_{232}t}$$

$$\times \left[ \begin{pmatrix} \frac{234\,\mathrm{U}}{238\,\mathrm{U}} \end{pmatrix}_{0} \frac{1}{\lambda_{234}} - \frac{\frac{f_{234}}{238\,\mathrm{U}_{0}}a_{238} + \frac{f_{238}}{238\,\mathrm{U}_{0}}\lambda_{238}}{\lambda_{238}a_{234}a_{238}} - \frac{a_{238} - \frac{f_{238}}{238\,\mathrm{U}_{0}}}{a_{238}(a_{234} - a_{238})} \right]$$

$$+ \begin{pmatrix} \frac{238\,\mathrm{U}}{232\,\mathrm{Th}} \end{pmatrix}_{0} \frac{\lambda_{230}\lambda_{234}}{\lambda_{230} - a_{238}} (e^{-a_{238}t} - e^{-\lambda_{230}t}) e^{\lambda_{232}t} \frac{a_{238} - \frac{f_{238}}{238\,\mathrm{U}_{0}}}{a_{234}a_{238}\lambda_{238}}$$

$$+ \begin{pmatrix} \frac{238\,\mathrm{U}}{232\,\mathrm{Th}} \end{pmatrix}_{0} \lambda_{234} \frac{\frac{f_{234}}{238\,\mathrm{U}_{0}}a_{238} + \frac{f_{238}}{238\,\mathrm{U}_{0}}\lambda_{238}}{a_{234}a_{238}\lambda_{238}} (1 - e^{-\lambda_{230}t}) e^{\lambda_{232}t}$$

$$+ \begin{pmatrix} \frac{234\,\mathrm{U}}{232\,\mathrm{Th}} \end{pmatrix}_{0} \lambda_{234} \frac{\frac{f_{234}}{238\,\mathrm{U}_{0}}a_{238} + \frac{f_{238}}{238\,\mathrm{U}_{0}}\lambda_{238}}{a_{234}a_{238}\lambda_{238}} (1 - e^{-\lambda_{230}t}) e^{\lambda_{232}t}$$

$$+ \begin{pmatrix} \frac{234\,\mathrm{U}}{232\,\mathrm{U}} \end{pmatrix}_{0} \lambda_{234} \frac{\frac{f_{234}}{238\,\mathrm{U}_{0}}a_{238} + \frac{f_{238}}{238\,\mathrm{U}_{0}}\lambda_{238}}{a_{234}a_{238}\lambda_{238}} - \frac{\lambda_{234}}{a_{234}a_{238}\lambda_{238}} e^{-a_{234}t}$$

$$+ \frac{\lambda_{234}}{238\,\mathrm{U}_{0}a_{238}} \frac{f_{238}}{238\,\mathrm{U}_{0}}e^{-a_{238}t} + \frac{\lambda_{234}}{238\,\mathrm{U}_{0}a_{238}} \frac{f_{238}}{238\,\mathrm{U}_{0}}a_{238} \frac{f_{238}}{238\,\mathrm{U}_{0}a_{238}} + \frac{\lambda_{234}}{238\,\mathrm{U}_{0}a_{238}} \frac{f_{238}}{238\,\mathrm{U}_{0}a_{238}} + \frac{\lambda_{234$$

and

$$a_{238} = \lambda_{238} + k_{238}$$
$$a_{234} = \lambda_{234} + k_{234}$$

where  $(^{238}\text{U}/^{232}\text{Th})_0$ ,  $(^{234}\text{U}/^{238}\text{U})_0$  and  $(^{230}\text{Th}/^{232}\text{Th})_0$  are initial activity ratios for the starting material such as unweathered core;  $^{238}\text{U}_0$  is the initial concentration of  $^{238}\text{U}$  in the starting material. To solve the model equations, we assume the addition and leaching terms  $(f_{238}, f_{234}, k_{238} \text{ and } k_{234})$  are constant in the rind over time.

The unknown parameters ( $f_{238}$ ,  $f_{234}$ ,  $k_{238}$  and  $k_{234}$ ) and individual rind formation ages (t) of a rind transect were solved with an inverse Monte Carlo modeling method (Mosegaard and Tarantola, 1995; Myung, 2003). The inverse Monte Carlo method is a variation of the standard Metropolis-Hasting algorithm to solve an inverse problem whereby parameters of a model are adjusted until its model results have the greatest consistency with experimental data. The consistency between the model results and the experimental data is assessed by using a maximum likelihood estimation (Myung, 2003).

Measured ( $^{238}\text{U}/^{232}\text{Th}$ ), ( $^{230}\text{Th}/^{232}\text{Th}$ ), and ( $^{234}\text{U}/^{238}\text{U}$ ) activity ratios in each rind sample are used to constrain the model. For the low-curvature rind transect, the model is constrained by 15 observations in the experimental data (238U/232Th, 230Th/232Th and 234U/238U activity ratios from 5 samples as data). The model fits 9 parameters (5 rind ages and  $f_{238}$ ,  $f_{234}$ ,  $k_{238}$ ,  $k_{234}$ ) to data. For the medium-curvature rind transect, the model is constrained by 12 observations in the experimental data ( $^{238}$ U/ $^{232}$ Th,  $^{230}$ Th/ $^{232}$ Th and <sup>234</sup>U/<sup>238</sup>U activity ratios from 4 samples as data). The model fits 8 parameters (4 rind ages and  $f_{238}$ ,  $f_{234}$ ,  $k_{238}$ ,  $k_{234}$ ) to data. For the high-curvature rind transect, the model is constrained by 9 observations in the experimental data (238U/232Th, 230Th/232Th and 234U/238U activity ratios from 3 samples as data). The model fits 7 parameters (3 rind ages and  $f_{238}$ ,  $f_{234}$ ,  $k_{238}$ ,  $k_{234}$ ) to data. In each case, the number of model constraining equations is greater than the number of unknowns, and thus the model is overdetermined.

For each rind transect, the inverse modeling method starts by randomly selecting a set of parameters  $(t_1, t_2, \ldots,$ and  $f_{238}$ ,  $f_{234}$ ,  $k_{238}$ ,  $k_{234}$ ) from a set of previously defined upper and lower bound of each parameter. The model results (y\_cal) calculated based on the randomly selected parameters by Eqs. C1-C3 were compared to the observed experiment data (y\_obs) and a likelihood function (Myung, 2003) was used to calculate the mismatch:  $\chi^2 = SUM$  $((y_cal - y_obs)^2/\sigma^2)$ , with the expected uncertainty  $\sigma$  as 2% of the experiment data. The standard Monte Carlo iteration algorithm (Mosegaard and Tarantola, 1995) was applied to repeat the above random selection process until a maximum likelihood estimation (minimum  $\chi^2$ ) was found within a maximum iteration number of 50,000. And the set of parameters  $(t_1, t_2, ..., and f_{238}, f_{234}, k_{238}, k_{234})$  at the maximum likelihood estimation represents one possible solution of the model. The above inverse Monte Carlo method was repeated for 100 times to get 100 sets of solutions at maximum likelihood estimation for each rind transect. The median and standard deviation of the 100 sets of solutions are used as the final solution and standard deviation of the model (Table 3). The model results for each of the 100 sets of solutions, as well as the median values of the 100 sets of solutions are shown in Figs. C1-C3.

The Matlab code for this inverse Monte Carlo method is attached below (Appendix D). These unknown parameters were solved in a similar manner to that of Dosseto et al. (2008a,b) and Ma et al. (2010, 2012). It is noted that in those previous studies, best-fit parameters were calculated with the Matlab™ *Isquonlin* function (version 7.1), which uses a large-scale algorithm to solve nonlinear least-

squares problems, instead of using the inverse Monte Carlo modeling with the maximum likelihood function.

### APPENDIX D

The Matlab code for the inverse Monte Carlo method

```
monte carlo inverse modeling(developed after Mosegaard and Tarantola;
and Myung papers)
% define y obs (e.g. 5 samples * 3 ratios = 15 obs)
%initial sample as the ave core
aTh230 U238 0 = 0.990;
aU234 \overline{U}238 \overline{0} = 1.003;
aU238 Th232 0 = 1.027;
% 5 samples
aU238 Th232 1 = 1.143;
aTh230_Th232_1 = 1.055;
aU234 U238 1 = 1.003;
d1 = \overline{1} \% mm
aU238 Th232 2 = 1.241;
aTh230_Th232_2 = 1.076;
aU234_U238_2 = 1.008;
d2 = 4.8; \% mm
aU238_Th232_3 = 1.342;
aTh230_Th232_3 = 1.131;
aU234_U238_3 = 1.014;
d3 = 7.5; %mm
aU238_Th232_4 = 1.279;
aTh230 Th232 4 = 1.132;
aU234 \overline{U}238 4 = 0.996;
d4 = 11.5; %mm
aU238_Th232_5 = 1.335;
aTh230_Th232_5 = 1.176;
aU234 U238 5 = 1.002;
d5 = \overline{15}; %mm
yobs= [aU238_Th232_1;
aTh230_Th232_1;
aU234_U238_1;
aU238 Th232 2;
aTh230 Th232 2;
aU234 U238 2;
aU238 Th232 3;
aTh230_Th232_3;
aU234_U238_3;
aU238_Th232_4;
aTh230 Th232 4;
aU234_U238_4;
aU238 Th232 5;
aTh230_Th232_5;
aU234_U238_5;
%define sigma measurement uncertainty
sigma = 0.02; % 2% of measured ratios
tn = 1;
tn all =1;
```

```
%define lower and upper bound of m vector (ts, fs and ks)
%m(1) time in years
%m(2) time in years
%m(3) time in years
%m(4) time in years
%m(5) time in years
m_1b(1) = 1;
m_ub(1) = 1250000;
m_1b(2) = 1;
m_ub(2) = 1250000;
m_1b(3) = 1;
m_ub(3) = 1250000;
m_lb(4) = 1;
m_ub(4) = 1250000;
m 1b(5) = 1;
m_ub(5) = 1250000;
%m(6) f238/238U0; atoms yr-1
%m(7) F234/F238 activity ratio
%m(8) k238; yr-1
%m(9) k234/k238
m_1b(6) = 0.01e-6;
m_ub(6) = 10e-5;
m lb(7) = 1;
m_ub(7) = 2;
m lb(8) = 0.01e-6;
m_{ub}(8) = 10e-5;
m lb(9) = 1;
m_ub(9) = 2;
%setup monte carlo
% pull random values for all m variables
%rand Uniformly distributed pseudorandom numbers
m_old = m_lb + (m_ub-m_lb).*rand(1,9);
%calculate ratios
ycal = mycalGua_time_234238leaching5(m_old, aTh230_U238_0,
aU234_U238_0, aU238_Th232_0);
% calculate likelihood function
chi2_old = sum((yobs-ycal).^2)/sigma^2;
S m old = sum((yobs-ycal).^2)/2;
```

```
for count = 1:1:50000
% pull a different value from 1 of the m variables randomly
%decide which m
i = randi(9);
m new = m old;
m \text{ new(i)} = m \text{ lb(i)} + (m \text{ ub(i)} - m \text{ lb(i)}) * rand();
% m new = m lb + (m ub-m lb).*rand(1,13);
m_all(tn_all, :) = m_new;
tn all = tn all+1;
ycal = mycalGua time 234238leaching5(m new, aTh230 U238 0,
aU234 U238 0, aU238 Th232 0);
% calculate likelihood function
chi2 new = sum((yobs-ycal).^2)/sigma^2;
S m new = sum((yobs-ycal).^2)/2;
%acceptance probability
if S m new <= S m old</pre>
   m_acceptance(tn,1:9) = m_new;
   m_acceptance(tn,10) = chi2_new;
   tn = tn + 1;
   m_old = m_new;
   S m old = S m new;
   \overline{\text{chi2}} old = \overline{\text{chi2}}_new;
else if rand() < exp(-(chi2_new-chi2_old)/2)</pre>
    m_acceptance(tn,1:9) = m_new;
   m_acceptance(tn,10) = chi2_new;
    tn = tn + 1;
   m_old = m_new;
   S m old = S m new;
   chi2_old = chi2_new;
end
end
[mm, mn] = size(m_acceptance);
s m = sortrows(m acceptance, mn);
result = s m(1,:);
```

Function *mycalGua\_time\_234238leaching5* is to calculate the three U-series activity ratios from Eq. (C1)–(C3) in Appendix C.

# REFERENCES

- Ames L. L., McGarrah J. E. and Walker B. A. (1983) Sorption of trace constituents from aqueous solutions onto secondary minerals. I Uranium. Clay Clay Mineral. 31, 321–334.
- Anderson S. P. (2005) Glaciers show direct linkage between erosion rate and chemical weathering fluxes. *Geomorphology* **67**, 147–157
- Andersson P. S., Porcelli D., Wasserburg G. J. and Ingri J. (1998) Particle transport of 234U–238U in the Kalix River and in the Baltic Sea. *Geochim. Cosmochim. Acta* 62, 385–392.

- Anderson S. P., Dietrich W. E. and Brimhall G. H. (2002) Weathering profiles, mass-balance analysis, and rates of solute loss: linkage between weathering and erosion in a small, steep catchment. *Geol. Soc. Am. Bull.* 114, 1143–1158.
- Andersen M. B., Erel Y. and Bourdon B. (2009) Experimental evidence for 234U–238U fractionation during granite weathering with implications for 234U/238U in natural waters. *Geochim. Cosmochim. Acta* 73, 4124–4141.
- Berner R. A., Lasaga A. and Garrels R. M. (1983) The carbonatesilicate geochemical cycle and its effect on atmospheric carbon dioxide over the past 100 million years. *Am. J. Sci.* **283**, 641–683.
- Bluth G. J. S. and Kump L. R. (1994) Lithologic and climatologic controls of river chemistry. *Geochim. Cosmochim. Acta* 58, 2341–2359.
- Bourdon B., Henderson G. M., Lundstrom C. C. and Turner S. P. (2003) Uranium-series Geochemistry. *Mineral. Soc. Am. Rev. Mineral. Geochem.* **52**, 656.

- Brantley S. L. and White A. F. (2009) Approaches to modeling weathered regolith. *Rev. Mineral. Geochem.* **70**, 435–484.
- Braun J.-J., Pagel M., Herbillon A. and Rosin C. (1993) Mobilization and redistribution of REEs and thorium in a syenitic lateritic profile: a mass balance study. *Geochim. Cosmochim. Acta* 57, 4419–4434.
- Brimhall G. H. and Dietrich W. E. (1987) Constitutive mass balance relations between chemical composition, volume, density, porosity, and strain in metosomatic hydrochemical systems: results on weathering and pedogenesis. *Geochim. Cosmochim. Acta* 51, 567–587.
- Buss H. L., Sak P. B., Webb S. M. and Brantley S. L. (2008) Weathering of the Rio Blanco quartz diorite, Luquillo Mountains, Puerto Rico: coupling oxidation, dissolution, and fracturing. *Geochim. Cosmochim. Acta* 72, 4488–4507.
- Buss H. L., White A. F., Dessert C., Gaillardet J., Blum A. E. and Sak P. B. (2010) Depth profiles in a tropical, volcanic critical zone observatory Basse-Terre, Guadeloupe. In *Water-Rock Interaction XIII* (eds. I. S. Torres-Alvarado and P. Birkle). CRC Press, pp. 245–248. http://dx.doi.org/10.1201/b10556-6.
- Carpentier M., Chauvel C. and Mattielli N. (2008) Pb–Nd isotopic constraints on sedimentary input into the Lesser Antilles arc system. *Earth Planet. Sci. Lett.* 272, 199–211.
- Cernohouz J. and Solc I. (1966) Use of sandstone wanes and weathered basaltic crust in absolute chronology. *Nature* 212, 806–807.
- Chabaux F., Riotte J. and Dequincey O. (2003a) U-Th-Ra fractionation during weathering and river transport. *Rev. Mineral. Geochem.* **52**, 533–576.
- Chabaux F., Dequincey O., Levesque J.-J., Leprun J.-C., Clauer N., Riotte J. and Paquet H. (2003b) Tracing and dating recent chemical transfers in weathering profiles by trace element geochemistry and 238U–234U–230Th disequilibria: the example of the Kaya lateritic toposequence (Burkina-Faso). *C. R. Geosci.* 335, 1219–1231.
- Chabaux F., Bourdon B. and Riotte J. (2008) U-series geochemistry in weathering profiles, river waters and lakes. *Radioact. Environ.* 13, 49–104.
- Chadwick O. A., Derry L. A., Vitousek P. M., Huebert B. J. and Hedin L. O. (1999) Changing sources of nutrients during four million years of ecosystem development. *Nature* 397, 491–497.
- Chamberlin T. C. (1898) An attempt to frame a working hypothesis of the cause of glacial periods on an atmospheric basis. *J. Geol.* 7, 545–584.
- Colman S. M. (1982a) Clay mineralogy of weathering rinds and possible implications concerning the sources of clay minerals in soil. *Geology* 10, 370–375.
- Colman, S.M. (1982b). Chemical weathering of basalts and basaltic andesites: evidence from weathering rinds. U.S.G.S. Professional Paper 1210. pp. 51.
- Colman, S.M., and Pierce, K.L. (1981). Weathering rinds on andesitic and basaltic stones as a Quaternary age indicator. Western United States. U.S. Geological Survey Professional Paper. pp. 41.
- Dequincey O., Chabaux F., Clauer N., Sigmarsson O., Liewig N. and Leprun J.-C. (2002) Chemical mobilizations in laterites: evidence from trace elements and 238U-234U-230Th disequilibria. *Geochim. Cosmochim. Acta* **66**, 1197-1210.
- Derry L. A., Kurtz A. C., Ziegler K. and Chadwick O. A. (2005) Biological control of terrestrial silica cycling and export fluxes to watersheds. *Nature* **433**, 728–731.
- Dessert C., Dupré B., Gaillardet J., Francois L. and Allègre C. J. (2003) Basalt weathering laws and the impact of basalt weathering on the global carbon cycle. *Chem. Geol.* 202, 257–273.

- Dessert C., Lajeunesse E., Lloret E., Clergue C., Crispi O., Gorge C. and Quidelleur X. (2015) Controls on chemical weathering on a mountainous volcanic tropical island: Guadeloupe (French West Indies). Geochim. Cosmochim. Acta 171, 216–237.
- Dosseto A., Bourdon B., Gaillardet J., Allegre C. J. and Filizola N. (2006) Timescale and conditions of chemical weathering under tropic climate: study of the Amazon basin with U-series. *Geochim. Cosmochim. Acta* 70, 71–89.
- Dosseto A., Bourdon B. and Turner S. P. (2008a) Uranium-series isotopes in river materials: insights into the timescales of erosion and sediment transport. *Earth Planet. Sci. Lett.* **265**, 1–17
- Dosseto A., Turner S. P. and Chappell J. (2008b) The evolution of weathering profiles through time: new insights from uranium-series isotopes. *Earth Planet. Sci. Lett.* **274**, 359–371.
- Dosseto A., Buss H. L. and Chabaux F. (2014) Age and weathering rate of sediments in small catchments: the role of hillslope erosion. *Geochim. Cosmochim. Acta* 132, 238–258.
- Drever J. I. and Stillings L. (1997) The role of organic acids in mineral weathering. *Colloids Surf. A* 120, 167–181.
- Duff M. C., Coughlin J. U. and Hunter D. B. (2002) Uranium coprecipitation with iron oxide minerals. *Geochim. Cosmochim.* Acta 66, 3533–3547.
- Dupre B., Dessert C., Oliva P., Godderis Y., Viers J., Francois L., Millot R. and Gaillardet J. (2003) Rivers, chemical weathering and Earth's climate. C. R. Geosci. 335, 1141–1160.
- Eiriksdottir E. S., Gislason S. R. and Oelkers E. H. (2013) Doe temperature or runoff control the feedback between chemical denudation and climate? Insights from NE Iceland. *Geochim. Cosmochim. Acta* **107**, 65–81.
- Fleischer R. L. (1980) Isotopic disequilibrium of uranium: alpharecoil damage and preferential solution effects. *Science* 207, 979–981.
- Gaillardet J., Dupré B., Louvat P. and Allègre C. J. (1999) Global silicate weathering and CO<sub>2</sub> consumption rates deduced from the chemistry of large rivers. *Chem. Geol.* 159, 3–30.
- Gaillardet J., Rad S., Rive K., Louvat P., Gorge C., Allegre C. J. and Lajeunesse R. (2011) Orography-driven chemical denudation in the Lesser Antilles: evidence for a new feed-back mechanism stabilizing atmospheric CO<sub>2</sub>. Am. J. Sci. 311, 851–894
- Gascoyne M. (1992) Geochemistry of the actinides and their daughters. In *Uranium-Series Disequilibrium: Application to Earth, Marine, and Environmental Sciences* (eds. M. Ivanovich and R. S. Harmon). Oxford Sciences Publications, Oxford, pp. 34-61
- Ghaleb B., Hillaire-Marcel C., Causse C., Gariepy C. and Vallieres S. (1990) Fractionation and recycling of U and Th isotopes in a semiarid endoreic depression of central Syria. *Geochim. Cos-mochim. Acta* 54, 1025–1035.
- Godsey S. E., Kirchner J. W. and Clow D. W. (2009) Concentration-discharge relationships reflect chemostatic characteristics of US catchments. *Hydrol. Proc.* 23, 1844–1864.
- Goldsmith S. T., Carey A. E., Johnson B. M., Welch S. A., Lyons W. B., McDowell W. H. and Pigott J. S. (2010) Stream geochemistry, chemical weathering and CO<sub>2</sub> consumption potential of andesitic terrains, Dominica, Lesser Antilles. *Geochim. Cosmochim. Acta* 74, 85–103.
- Gordon S. J. and Dorn R. I. (2005) In situ weathering rind erosion. *Geomorphology* **67**, 97–113.
- Graham R. C., Rossi A. M. and Hubbert K. R. (2010) Rock to regolith conversion: producing hospitable substrates for terrestrial ecosystems. GSA Today 20, 4–9.
- Granet M., Chabaux F., Stille P., France-Lanord C. and Pelt E. (2007) Time-scales of sedimentary transfer and weathering

- processes from U-series nuclides: clues from the Himalayan rivers. *Earth Planet. Sci. Lett.* **261**, 389–406.
- Granet M., Chabaux F., Stille P., Dosseto A., France-Lanord C. and Blaes E. (2010) U-series disequilibria in suspended river sediments and implication for sediment transfer time in alluvial plains: the case of the Himalayan rivers. *Geochim. Cosmochim. Acta* 74, 2851–2865.
- Hausrath E. M., Navarre-Sitchler A. K., Sak P. B., Steefel C. I. and Brantley S. L. (2008) Basalt weathering rates on Earth and the duration of liquid water on the plains of Gusev Crater. *Mars Geol.* 36(1), 67–70.
- Hawkesworth C. J. and Powell M. (1980) Magma genesis in the lesser Antilles island arc. *Earth Planet. Sci. Lett.* **51**, 297–308.
- Hilley G. E. and Porder S. (2008) A framework for predicting global silicate weathering and CO<sub>2</sub> drawdown rates over geological time-scales. *PNAS* **105**, 16855–16859.
- Hilley G. E., Chamberlain C. P., Moon S. G., Porder S. and Willett S. (2010) Competition between erosion and reaction kinetics in controlling silicate weathering rates. *Earth Planet. Sci. Lett.* 293, 191–199.
- Hren M. T., Chamberlin C. P., Hilley G. E., Blisniuk P. M. and Bookhagen B. (2007) Major ion chemistry of the Yarlung Tsangpo-Brahmaputra river: chemical weathering, erosion, and CO<sub>2</sub> consumption in the southern Tibetan plateau and eastern syntaxis of the Himalaya. *Geochim. Cosmochim. Acta* 71, 2907– 2935.
- Ivanovich M. and Harmon R. S. (1992) Uranium-series Disequilibrium: Applications to Earth, Marine, and Environmental Sciences. Clarendon Press, Oxford.
- Jacobson A. D., Blum J. D., Chamberlain C. P., Craw D. and Koons P. O. (2003) Climatic and tectonic controls on chemical weathering in the New Zealand Southern Alps. *Geochim. Cosmochim. Acta* 67, 29–46.
- Jordan T. H. (1975) The present-day motion of the Caribbean plate. *J. Geophys. Res.* **80**, 4433–4439.
- Kirkbride M. P. and Bell C. M. (2010) Edge-roundness of boulders of Torridonian Sandstone (northwest Scotland): applications for relative dating and implications for warm and cold climate weathering rates. *Boreas* 39, 187–198.
- Lahitte P., Samper A. and Quidelleur X. (2012) DEM-based reconstruction of southern Basse-Terre volcanoes (Guadeloupe archipelago, FWI): contribution to the Lesser Antilles Arc construction rates and magma production. *Geomorphology* 136, 148–164
- Latham A. G. and Schwarcz H. P. (1987a) On the possibility of determining rates of removal of uranium from crystalline igneous rocks using U-series disequilibria 1: a U-leach model, and its applicability to whole-rock data. *Appl. Geochem.* **2**, 55–65.
- Latham A. G. and Schwarcz H. P. (1987b) On the possibility of determining rates of removal of uranium from crystalline igneous rocks using U-series disequilibria 2: applicability of a U-leach model to mineral separates. *Appl. Geochem.* 2, 67–71
- Lebedeva M. I., Fletcher R. C., Balashov V. N. and Brantley S. L. (2007) A reactive-diffusion model describing transformation of bedrock to saprolite. *Chem. Geol.* 244, 624–645.
- Lebedeva M. I., Fletcher R. C., Brantley S. and 554 L. (2010) A mathematical model of steady state regolith production at constant erosion rate. *Earth Surf. Proc. Land.* **35**, 508–524.
- Lebedeva M. I., Sak P. B., Ma L. and Brantley S. L. (2015) Using a mathematical model of a weathering clast to explore the effects o curvature on weathering. *Chem. Geol.* 404, 88–99.
- Lichtner P. C. (1988) The quasi-stationary state approximation to coupled mass transport and fluid–rock interaction in a porous medium. *Geochim. Cosmochim. Acta* **52**, 143–165.

- Lloret E., Dessert C., Gaillardet J., Alberic P., Crispi O., Chaduteau C. and Benedetti M. F. (2011) Comparison of dissolved inorganic and organic carbon export in the rivers of tropical volcanic island; example from Guadeloupe, French West Indies. Chem. Geol. 280, 65–78.
- Lloret E., Dessert C., Pastor L., Lajeunesse E., Crispi O., Gaillardet J. and Bebedetti M. F. (2013) Dynamic of particulate and dissolved organic carbon in small volcanic mountainous tropical watersheds. *Chem. Geol.* 351, 229–244.
- Louvat P. and Allègre C. J. (1997) Present day denudation rates of the Islnad of Réunion determined by river geochemistry: basalt weathering and mass budgets between chemical and mechanical erosions. *Geochim. Cosmochim. Acta* 61, 3645–3669.
- Ma J.-L., Wei G.-J., Xu Y.-G., Long W.-G. and Sun W.-D. (2007) Mobilization and re-distribution of major and trace elements during extreme weathering of basalt in Hainan Island, South China. Geochim. Cosmochim. Acta 71, 3223–3237.
- Ma L., Chabaux F., Pelt E., Blaes E., Jin L. and Brantley S. L. (2010) Regolith production rates calculated with uranium-series isotopes at Susquehanna/Shale Hills Critical Zone Observatory. *Earth Planet. Sci. Lett.* 297, 211–225.
- Ma L., Chabaux F., Pelt E., Granet M., Sak P. B., Gaillardet J., Lebedeva M. and Brantley S. L. (2012) The effect of curvature on weathering rind formation: evidence from Uranium-series isotopes in basaltic andesite weathering clasts in Guadeloupe. *Geochim. Cosmochim. Acta* 80, 92–107.
- Maher K. (2010) The dependence of chemical weathering rates on fluid residence time. *Earth Planet. Sci. Lett.* **294**, 101–110.
- Maher K. and Chamberlain C. P. (2014) Hydrologic regulation of chemical weathering and the geological carbon cycle. *Science* **343**, 1502. http://dx.doi.org/10.1126/science.1250770.
- Maher K., DePaolo D. J. and Lin J. C. F. (2004) Rates of silicate dissolution in deep-sea sediment: In situ measurement using U-234/U-238 of pore fluids. *Geochim. Cosmochim. Acta* 68, 4629– 4648.
- Maher K., Steefel C. I., DePaolo D. J. and Viani B. E. (2006) The mineral dissolution rate conundrum: insights from reactive transport modeling of U isotopes and pore fluid chemistry in marine sediments. *Geochim. Cosmochim. Acta* 70, 337–363.
- Millot R., Gaillardet J., Dupre B. and Allegre C. J. (2002) The global control of silicate weathering rates and the coupling with physical erosion: new insights from rivers of the Canadian Shield. *Earth Planet. Sci. Lett.* **196**, 83–98.
- Mosegaard K. and Tarantola A. (1995) Monte Carlo sampling of solutions to inverse problems. *J. Geophys. Res.* **100**, 12431–12447.
- Myung I. J. (2003) Tutorial on maximum likelihood estimation. *J. Math. Psychol.* **47**, 90–100.
- Navarre-Sitchler A. and Brantley S. (2007) Basalt weathering across scales. *Earth Planet. Sci. Lett.* 261, 321–334.
- Navarre-Sitchler A., Steefel C., Tomutsa L., Yang L. and Brantley S. L. (2009) Evolution of porosity and diffusivity during chemical weathering of a basalt clast. J. Geophys. Res. Earth Surf. 114, F02016. http://dx.doi.org/10.1029/2008JF001060.
- Navarre-Sitchler A., Steefel C., Sak P. and Brantley S. L. (2011) A predictive model for weathering rind formation on basalt. *Geochim. Cosmochim. Acta* 75, 7644–7667.
- Ndayiragije S. and Delvaux B. (2004) Selective sorption of potassium in a weathering sequence of volcanic ash soils from Guadeloupe, French West Indies. *Catena* **56**(1–3), 185–198.
- Neaman A., Chorover J. and Brantley S. L. (2006) Effects of organic ligands on granite dissolution in batch experiments at pH 6. Am. J. Sci. 306, 451–473.
- Nugent M. A., Brantley S. L., Pantano C. G. and Maurice P. A. (1998) The influence of natural mineral coatings on feldspar weathering. *Nature* 395, 588–591.

- Oguchi C. T. and Matsukura Y. (2000) Effect of porosity on the increase in weathering-rind thicknesses of basaltic andesite gravel. Eng. Geol. 55, 77–89.
- Pacheco F. A. L. and Alencoao A. M. P. (2006) Role of fractures in weathering of solid rocks: narrowing the gap between laboratory and field weathering rates. *J. Hydrol.* 316, 248–265.
- Pelt E., Chabaux F., Innocent C., Navarre-Sitchler A. K., Sak P. B. and Brantley S. L. (2008) Uranium-thorium chronometry of weathering rinds: rock alteration rate and paleo-isotopic record of weathering fluids. *Earth Planet. Sci. Lett.* 276, 98–105.
- Pereyra Y. (2016) Uranium-series and strontium isotope ratios in soils from Basse-Terre Island, French Guadeloupe: Insights for rapid soil formation and impact of dust in a tropical volcanic setting MS thesis. University of Texas, El Paso, p. 91.
- Plater A. J., Ivanovich M. and Dugdale R. E. (1992) Uranium series disequilibrium in river sediments and waters: the significance of anomalous activity ratios. *Appl. Geochem.* 7, 101–110.
- Porter S. C. (1975) Weathering rinds as a relative-age criterion: application to subdivision of glacial deposits in the Cascade Range. *Geology* 3, 101–104.
- Raymo M. E. and Ruddiman W. F. (1992) Tectonic forcing of late Cenozoic climate. *Nature* **10**, 117–122.
- Reeves D. and Rothman D. H. (2014) Diffusion and kinetic control of weathering layer development. *Geofluids* **14**, 128–142.
- Ricci J., Lahitte P. and Quidelleur X. (2015) Construction and destruction rates of volcanoes within a tropical environment based on K-Ar dating and numerical reconstructions: examples from the Basse-Terre Island (Guadeloupe, Lesser Antilles). Geomorphology 228, 597–607.
- Rosholt J., Doe B. and Tatsumoto M. (1966) Evolution of the isotopic composition of uranium and thorium in soil profiles. *Geol. Soc. Am. Bull.* 77, 987–1004.
- Rossi A. M. and Graham R. C. (2010) Weathering and porosity formation in subsoil granitic clasts, Bishop Creek Moraines, California. Soil Sci. Soc. Am. J. 74, 172–185.
- Rousteau A. (1996) Structures, flores, dynamiques: réponses des forêts pluviales des Petites Antilles aux milieux montagnards. In *Phytogéographie tropicale: réalités et perspectives* (eds. J. L. Guillaumet, M. Belin and H. Puig). ORSTOM, Paris.
- Sak P. B., Fisher D. M., Gardner T. W., Murphy K. and Brantley S. L. (2004) Rates of weathering rind formation on Costa Rican basalt. *Geochim. Cosmochim. Acta* 68, 1453–1472.
- Sak P. B., Navarre-Sitchler A. K., Miller C. E., Daniel C. C., Gailardet J., Buss H. L., Lebedeva M. I. and Brantley S. L. (2010) Controls on rind thickness on basaltic andesite clasts weathering in Guadeloupe. *Chem. Geol.* 276, 129–143.
- Samper A., Quidelleur X., Lahitte P. and Mollex D. (2007) Timing of effusive volcanism and collapse events within an oceanic arc island: Basse-Terre, Guadeloupe archipelago (Lesser Antilles Arc). Earth Planet. Sci. Lett. 258, 175–191.
- Sarin M. M., Krishnaswami S., Somayajulu B. L. K. and Moore W. S. (1990) Chemistry of uranium, thorium, and radium

- isotopes in the Ganga-Brahmaputra river system weathering processes and fluxes to the Bay of Bengal. *Geochim. Cosmochim. Acta* **54.** 1387–1396.
- Shirvington P. J. (1983) Fixation of radionuclides in the 238U decay series in the vicinity of mineralized zones: 1. The Austatom Uranium Prospect, Northern Territory, Australia. Geochim. Cosmochim. Acta 47, 403–412.
- Sims K. W. W., Gill J. B., Dosseto A., Hoffmann D. L., Lundstrom C. C., Williams R. W., Ball L., Tollstrup D., Turner S., Prytulak J., Glessner J. G., Standish J. J. and Elliott T. (2010) An inter-laboratory assessment of the thorium isotopic composition of synthetic and rock reference materials. *Geostand. Geoanal. Res.* 32, 65–91.
- Velbel M. A. (1993) Constancy of silicate–mineral weathering-rate ratios between natural and experimental weathering: implications for hydrologic control of differences in absolute rates. *Chem. Geol.* 105, 89–99.
- Vigier N., Bourdon B., Turner S. and Allegre C. J. (2001) Erosion timescales derived from U-decay series measurements in rivers. *Earth Planet. Sci. Lett.* 193, 485–499.
- Walker J., Hays P. and Kasting J. (1981) A negative feedback mechanism for the long-term stabilization of Earth's surface temperature. J. Geophys. Res. 86, 9776–9782.
- Wasklewicz T. A. (1994) Importance of environment on the order of mineral weathering in olivine basalts, Hawaii. *Earth Surf. Process. Land.* 19, 715–734.
- West A. J., Galy A. and Bickle M. (2005) Tectonic and climatic controls on silicate weathering. Earth Planet. Sci. Lett. 235, 211–238
- White W. M. (2014) Geochemistry. Wiley-Blackwell, Oxford, UK, p. 660.
- White A. F. and Brantley S. L. (2003) The effect of time on the weathering of silicate minerals: why do weathering rates differ in the laboratory and field? *Chem. Geol.* 202, 479–506.
- White A. F., Blum A. E., Schulz M. S., Vivit D. V., Stonestrom D.
  A., Larsen M., Murphy S. F. and Eberl D. (1998) Chemical weathering in a tropical watershed, Luquillo Mountains, Puerto Rico: I. Long-term versus short-term weathering fluxes. *Geochim. Cosmochim. Acta* 62, 209–226.
- Yoshida H., Metcalfe R., Nishimoto S., Yahamamoto H. and Katsuta N. (2011) Weathering rind formation in buried terrace cobbles during periods of up to 300 ka. *Appl. Geochem.* 26, 1706–1721. http://dx.doi.org/10.1016/j. apgeochem.2011.04.027.
- Zhu C. (2009) Geochemical modeling of reaction paths and geochemical reaction networks. Zhu C Chap. 12 in thermodynamics and kinetics of water-rock interactions. Rev. Mineral. Geochem. 70(1), 533-569.

Associate editor: Anthony Dosseto